Novel axonemal protein ZMYND12 interacts with TTC29 and DNAH1, and is required for male fertility and flagellum function.

Denis Dacheux[1,2,18], Guillaume Martinez[3,4,18], Christine E. Broster Reix[1], Julie Beurois[4], Patrick Lorès[5], Magamba Tounkara[1], Jean-William Dupuy[6], Derrick R. Robinson[1,2], Corinne Loeuillet[4], Emeline Lambert[4], Zeina Wehbe[4], Amir Amiri-Yekta[7], Abbas Daneshipour[7], Seyedeh-Hanieh Hosseini[8], Raoudha Zouari[9], Sélima Fourati Ben Mustapha[9], Lazhar Halouani[9], Xiaohui Jiang[10,11,12], Ying Shen[11,12], Chunyu Liu[13], Nicolas Thierry-Mieg[14], Amandine Septier[14], Marie Bidart[4,15], Véronique Satre[3,4], Caroline Cazin[4,16], Zine-Eddine Kherraf[4,16], Christophe Arnoult[4], Pierre F. Ray[4,16], Aminata Touré[17,19], Mélanie Bonhivers[1,19] and Charles Coutton[3,4,19,*]

[1] Univ. Bordeaux, CNRS, MFP, UMR 5234, F-33000 Bordeaux, France.
[2] Bordeaux INP, Microbiologie Fondamentale et Pathogénicité, UMR 5234, F-33000 Bordeaux, France.
[3] CHU Grenoble Alpes, UM de Génétique Chromosomique, 38000 Grenoble, France.
[4] Institute for Advanced Biosciences, INSERM U1209, CNRS UMR 5309, Univ. Grenoble Alpes, Team Genetics Epigenetics and Therapies of Infertility, 38000 Grenoble, France.
[5] Institut Cochin, INSERM U1016, CNRS UMR 8104, Université Paris Cité, 75014 Paris, France.
[6] Univ. Bordeaux, Plateforme Protéome, F-33000, Bordeaux, France.
[7] Department of Genetics, Reproductive Biomedicine Research Center, Royan Institute for Reproductive Biomedicine, ACECR, Tehran-Iran.
[8] Department of Andrology, Reproductive Biomedicine Research Center, Royan Institute for Reproductive Biomedicine, ACECR, Tehran-Iran.
[9] Polyclinique les Jasmins, Centre d'Aide Médicale à la Procréation, Centre Urbain Nord, Tunis, Tunisia.
[10] Human Sperm Bank, West China Second University Hospital of Sichuan University, Chengdu, Sichuan, China.
[11] NHC Key Laboratory of Chronobiology, Sichuan University, Chengdu, Sichuan, China.
[12] Key Laboratory of Birth Defects and Related Diseases of Women and Children (Sichuan University), Ministry of Education, China.
[13] Obstetrics and Gynecology Hospital, Fudan University, Shanghai, China.
[14] Univ. Grenoble Alpes, CNRS, UMR5525, TIMC, 38000 Grenoble, France.
[15] CHU Grenoble Alpes, Laboratoire de Génétique Moléculaire: Maladies Héréditaires et Oncologie, Grenoble, France.
[16] CHU de Grenoble, UM GI-DPI, Grenoble, 38000, France.
[17] Institute for Advanced Biosciences, INSERM U 1209, CNRS UMR 5309, Université Grenoble Alpes, Team Physiology and Pathophysiology of Sperm cells 38000 Grenoble, France.
[18] These authors contributed equally to this work.
[19] These authors contributed equally to this work.

*Correspondence: CCoutton@chu-grenoble.fr

ABSTRACT

Male infertility is common and complex, presenting a wide range of heterogeneous phenotypes. Although about 50% of cases are estimated to have a genetic component, the underlying cause often remains undetermined. Here, from whole-exome sequencing on samples from 168 infertile men with asthenoteratozoospermia due to severe sperm flagellum, we identified homozygous *ZMYND12* variants in four unrelated patients. In sperm cells from these individuals, immunofluorescence revealed altered localization of DNAH1, DNALI1, WDR66 and TTC29. Axonemal localization of ZMYND12 ortholog TbTAX-1 was confirmed using the *Trypanosoma brucei* model. RNAi knock-down of TbTAX-1 dramatically affected flagellar motility, with a phenotype similar to the sperm from men bearing homozygous *ZMYND12* variants . Co-immunoprecipitation and ultrastructure expansion microscopy in *T. brucei* revealed TbTAX-1 to form a complex with TTC29. Comparative proteomics with samples from *Trypanosoma* and *Ttc29* KO mice identified a third member of this complex: DNAH1. The data presented revealed that ZMYND12 is part of the same axonemal complex as TTC29 and DNAH1, which is critical for flagellum function and assembly in humans, and Trypanosoma. ZMYND12 is thus a new asthenoteratozoospermia-associated gene, bi-allelic variants of which cause severe flagellum malformations and primary male infertility.

Keywords: asthenoteratozoospermia / male infertility / MMAF / sperm flagellum / ZMYND12

INTRODUCTION

Male infertility is one of the most challenging health issues that will face us in the near future. Recent decades have been marked by a significant and constant deterioration of quantitative and qualitative sperm parameters in both humans and animals, demonstrating the detrimental impact of recent environmental changes (Rolland et al., 2013). However, environmental factors are not the sole cause of male infertility, which is often multifactorial. Among the various possible causes, it is estimated that a genetic component, alone or in association, can be found in about half of cases (Oud et al., 2022).

Spermatozoa are the most highly differentiated and specialized human cells, as reflected by the 2,300 genes necessary for normal spermatogenesis (Lu et al., 2019). The complex process of spermatogenesis is divided into three phases: proliferation and differentiation of spermatogonia, meiosis, and the final critical step, spermiogenesis. During spermiogenesis, haploid round spermatids undergo an extraordinary series of transformations to acquire the specific morphological features necessary for them to competently fertilize an egg. The stages in spermiogenesis include nuclear compaction, acrosome formation and flagellum biogenesis (O'Donnell, 2014). Any defects in genes driving these differentiation steps can lead to severe functional or morphological sperm defects, and thus male infertility.

Interestingly, the prevalence of genetic defects is higher in conditions with severe sperm phenotypes (Coutton et al., 2015). Multiple Morphological Abnormalities of the sperm Flagellum (MMAF) is a condition associated with extreme morphological sperm defects characterized by a mosaic of phenotypes. Thus, MMAF sperm cells may lack a flagellum or bear a short, irregular, or coiled flagellum. Because of these characteristics, MMAF causes total asthenozoospermia with almost no progressive sperm (Touré et al., 2020). At the ultrastructural level, MMAF is associated with severe disorganization of both axonemal and peri-axonemal

structures (Nsota Mbango et al., 2019). Approximately 40 genes have been strongly or definitively associated with the MMAF phenotype so far (Wang et al., 2020). However, this high genetic heterogeneity means the prevalence of individual variants of each gene remains low, and the underlying genetic component remains unknown for about half of affected individuals. It is therefore necessary to pursue the identification of new candidate MMAF genes to increase the diagnostic yield and improve our understanding of the pathophysiological mechanisms inducing this sperm phenotype. In addition, the identification of MMAF genes provides invaluable clues to the molecular mechanisms underlying sperm flagellum biogenesis. Therefore, efforts are continuously being deployed to decipher the precise organization, localization and interactions of each protein encoded by these genes within the flagellum.

Here, following analysis of an initial cohort of 167 MMAF individuals by whole-exome sequencing (WES), we identified truncating homozygous variants in *ZMYND12* in three unrelated individuals. A fourth individual with a similar mutation was subsequently identified in a Chinese cohort. In this paper, we present a thorough investigation of the role of this new gene by studying its ortholog, TbTAX-1, in *Trypanosoma*, an evolutionarily-distant model sharing a highly conserved flagellar structure. We first showed the importance of ZMYND12 for the axonemal structure and function of the flagellum. Subsequently, we shed light on ZMYND12 function in the flagellum using the TbTAX-1 protist model and *Ttc29* KO mice. Results formally demonstrated that ZMYND12 interacts directly with DNAH1 and TTC29 (two known MMAF-related proteins) within the same axonemal complex.

RESULTS

Whole-exome sequencing (WES) identified homozygous truncating variants in *ZMYND12* in MMAF individuals.

In our cohort of 167 MMAF individuals, we previously identified 83 individuals (49.7%) with harmful gene variants in known MMAF-related genes. Reanalysis of the remaining negative exomes identified three unrelated MMAF individuals (ZMYND12$_{_1\text{-}3}$) (Fig. 1A, Table 1) carrying homozygous variants in *ZMYND12* (Zinc Finger MYND-Type Containing 12, NM_032257.5). This gene was not previously associated with any pathology. Two individuals (ZMYND12$_{_1}$ and ZMYND12$_{_3}$) originated from Tunisia, and one individual (ZMYND12$_{_2}$) was of Iranian origin.

ZMYND12 is located on chromosome 1 and contains eight exons encoding the Zinc finger MYND domain-containing protein 12, a predicted 365-amino acid protein (Q9H0C1). According to data from GTEx, *ZMYND12* is strongly expressed in the testis and is associated with cilia and flagella (Yamamoto et al., 2021, 2006). Moreover, quantitative single-cell RNA sequencing datasets from human adult testis (ReproGenomics Viewer) (Darde et al., 2019) indicate abundant expression in germ cells from zygotene spermatocyte to late spermatid stages. This expression pattern suggests a role in sperm cell differentiation and/or function. ZMYND12 protein was also detected at significant levels in the human sperm proteome (Wang et al., 2013), but at very low levels in human airway cilia (Blackburn et al., 2017). We performed RT-qPCR experiments on human tissue panels (Fig. S1), and results confirmed that expression of *ZMYND12* mRNA is predominant in testis as compared with the other tissues tested.

A stop-gain variant c.433C>T; p.Arg145Ter (NM_032257.5, GRCh38 g.chr1:42440017G>A, rs766588568), located in *ZMYND12* exon 4 (Fig. 1B), was identified in individuals ZMYND12$_{_1}$ and ZMYND12$_{_3}$. Subsequently, a Chinese MMAF subject harboring

the same homozygous stop-gain variant in *ZMYND12* (ZMYND12_4) was identified in the cohort collected by the Human Sperm Bank of West China Second University Hospital of Sichuan University hospital (Fig. 1, Table 1). This c.433C>T variant is present in the Genome Aggregation Database (gnomAD v2.1.1, http://gnomad.broadinstitute.org/variant/1-42905688-G-A) database with a minor allele frequency (MAF) of 3.391e-05. This nonsense variant, identified by exome sequencing, was confirmed by Sanger sequencing in all four individuals (Fig. 1C).

Using the ExomeDepth software package (Plagnol et al., 2012), individual ZMYND12_2, was identified based on a homozygous deletion removing *ZMYND12* exons 6, 7 and 8 (Fig. S2). We confirmed the presence of the homozygous deletion in the affected individual by custom MLPA (Fig. 1D). The deletion identified was not listed in public databases, including DECIPHER (https://www.deciphergenomics.org/) and the Database of Genomic Variants (http://dgv.tcag.ca/dgv/app/home).

For the individuals carrying *ZMYND12* mutations, analysis of control databases revealed no low-frequency variants in other genes reported to be associated with cilia, flagella or male fertility. We therefore focused our study on *ZMYND12*, which appeared as the best MMAF candidate gene. All of the *ZMYND12* variants identified here have been deposited in ClinVar under reference SUB12540308.

ZMYND12 is located in the sperm flagellum, its variants cause severe axonemal disorganization

To further investigate the pathogenicity of the *ZMYND12* variants identified, we examined the distribution of the ZMYND12 protein in control and mutated sperm cells by immunofluorescence (IF). Due to sample availability, these analyses were only carried out for

individual ZMYND12_3 – carrier of the recurrent stop-gain variant c.433C>T. In sperm from control individuals, ZMYND12 antisera decorated the full length of the sperm flagellum (Fig. 1E). Conversely, and in line with a truncation or degradation of the mutated protein, ZMYND12 was totally absent from all sperm cells from individual ZMYND12_3 (Fig. 1E). Importantly, ZMYND12 was detected in sperm cells from MMAF individuals bearing mutations in other genes (*ARMC2* and *WDR66*) or with unknown genetic causes (Fig. S3). Thus, the absence of ZMYND12 is not a common feature of the MMAF phenotype, and is specifically associated with *ZMYND12* variants.

To explore the ultrastructural defects induced by *ZMYND12* variants in human sperm cells, we next studied the presence of proteins present in various axonemal and peri-axonemal substructures by IF. The following proteins were investigated: AKAP4 (fibrous sheath, FS), CFAP70 (axoneme-binding protein with unknown precise location), DNAI1 (outer arm intermediate chain), DNALI1 (inner arm light intermediate chain), DNAH1 (inner arm heavy chain), DNAH8 (outer arm heavy chain), DNAH17 (outer arm heavy chain), GAS8 (Nexin-Dynein Regulatory Complex, N-DRC), RSPH1 (radial spoke, RS), SPAG6 (central pair complex, CPC), WDR66/CFAP251 (calmodulin-associated and spoke-associated complex, CSC), and TTC29 (axoneme-binding protein with unknown precise location). In sperm cells from ZMYND12_3, we first observed a total lack of SPAG6 staining (Fig. S4A), suggesting severe CPC defects. This type of defect is a common feature of MMAF spermatozoa (Coutton et al., 2015). In addition, no immunostaining for DNAH1, DNALI1, or WDR66 was detected in sperm from individual ZMYND12_3 (Fig. 2A, 2B and S4B). These results suggested a strong disorganization of the IDAs and the CSC. ZMYND12 could therefore be a key axonemal component responsible for stability of these structures.

We subsequently examined the presence of TTC29 and CFAP70, two proteins with as yet incompletely characterized function and localization. In control sperm, TTC29 and CFAP70

immunostaining decorated the full length of the flagellum, but neither protein was detected in cells from individual ZMYND12_3 (Fig. 2C and 2D). Intriguingly, ZMYND12 was undetectable in the sperm flagellum from an MMAF individual carrying a previously-reported *TTC29* splicing variant c.1761+1G>A (Lorès et al., 2019) (Fig. S5). Unfortunately, no sample from an individual carrying a bi-allelic *CFAP70* variant could be analyzed. Nevertheless, the available data suggest that TTC29, CFAP70, and ZMYND12 may be physically or functionally associated within the same axonemal complex.

We also observed heterogeneous RSPH1 staining with all flagellar morphologies (Fig. S6), indicating that radial spokes are inconsistently present in sperm cells from individual ZMYND12_3. In contrast, the immunostaining patterns for AKAP4, DNAH8, DNAH17, DNAI1, and GAS8 were comparable to those observed in control sperm cells. This result indicates that the fibrous sheath (FS), the outer dynein arms (ODAs), and the N-DRC were not directly affected by *ZMYND12* variants (Fig. S7). Transmission Electron Microscopy (TEM), which could provide direct evidence of ultrastructural defects, could not be performed due to the very low number of sperm cells available from *ZMYND12* individuals.

TbTAX-1, the *Trypanosoma brucei* ortholog of ZMYND12, is an axoneme-associated protein involved in flagellar motility

To validate our candidate gene and better characterize ZMYND12 localization and function, we used the Trypanosoma model. Forward and reverse genetic approaches are well established for this model, and have largely contributed to the characterization of the molecular pathogenesis of a number of human diseases caused by defective cilia and/or flagella (Vincensini et al., 2011). BlastP analysis of the *Trypanosoma brucei* genome database (Aslett et al., 2010) identified the putative ortholog of ZMYND12 as Tb927.9.10370. The *T. brucei* gene encodes TbTAX-1, a 363 amino acid protein previously identified by proteomics analyses

as a flagellar protein, annotated as the inner dynein arm protein/p38 (FAP146) (Broadhead et al., 2006; Ralston et al., 2009). Human ZMYND12 (Q9H0C1) and TbTAX-1 share 29% protein identity and 48% similarity. Both proteins contain a TPR motif domain potentially involved in protein-protein interaction (D'Andrea and Regan, 2003) (Fig. S8A and B).

RNAi knock-down of TbTAX-1 in the bloodstream form (BSF) of *T. brucei* is reported to lead to multi-flagellated cells, suggesting incomplete cell division (Broadhead et al., 2006). This phenotype is described when proteins directly or indirectly involved in flagellar motility are knocked down in the BSF (Coutton et al., 2018; Ralston et al., 2011). In contrast, in the procyclic form, knock-down induces cell sedimentation due to motility defects (Baron et al., 2007).

Here, to analyze the protein's localization by immunofluorescence (IF) on detergent-extracted cells (cytoskeletons, CSK), we generated a procyclic *T. brucei* cell line endogenously expressing myc-tagged TbTAX-1 ($_{myc}$TbTAX-1). $_{Myc}$TbTAX-1 specifically localized to the flagellum, as shown by co-staining with the Paraflagellar Rod-2 protein (PFR2), a marker of the para-axonemal and axoneme-associated structure (PFR) (Fig. 3A). Importantly, $_{Myc}$TbTAX-1 was found to associate with the axoneme fraction of the flagellum, with staining observed in the distal part of the flagellum, beyond the limit of PFR labeling (Fig. 3A). Furthermore, mycTbTAX-1 labeling was observed in both the old flagellum and the new flagellum, indicating that the protein is present at all stages of the cell cycle, in line with proteomics data reported for the Trypanosoma cell cycle (Crozier et al., 2018).

Trypanosoma brucei TAX-1 is involved in flagellum motility

To assess the functional role of TbTAX-1 in the procyclic parasite model, we used a tetracycline-inducible RNA interference (RNAi) system (Wirtz et al., 1999) to knock-down TbTAX-1 expression. Using the $_{myc}$TbTAX-1 / TbTAX-1^{RNAi} *T. brucei* cell line (Fig. 3), we

observed the effects of TbTAX-1 knock-down following the addition of tetracycline. Western blot analysis confirmed successful RNA interference, leading to a significant reduction in TbTAX-1 protein levels (Fig. 3B). These results were confirmed by IF, where expression of $_{Myc}$TbTAX-1 was strongly reduced in the new flagellum (NF) compared to the old flagellum (OF) (Fig. 3C). Comparison of TEM images of thin sections from wild-type (WT) and RNAi-induced cells after 7 days revealed no obvious differences in flagellum ultrastructure (Fig. S9), and TbTAX-1 knock-down had no effect on cell growth (Fig. 3D). However, video microscopy evidence pointed to a strong mobility defect (Movies S1 and S2). Tracking analysis (Fig. 3E) indicated that reduced mobility was linked to problems with flagellar beating. In line with these observations, sedimentation assays showed that after induction for 48 h, 70% of RNAi-induced cells had sedimented (Fig. 3F).

The truncated TbTAX-1 protein is not associated with the flagellum and cannot rescue the motility defect induced by TbTAX-1 RNAi

The p.Arg145Ter mutation of *ZYMND12* identified in MMAF individuals could theoretically produce a truncated form of the protein (aa 1-144). To assess where a similar truncated protein – TbTAX-1 (aa 1-128) – would localize, we generated a TAX-1$_{HA}$ *Trypanosoma* cell line expressing the truncated form TbTAX-1$^{Trunc}_{Ty1}$ alongside the tagged full-length form. The relative sizes of the mutated, truncated ZMYND12 protein potentially encoded in human patients and the equivalent modified, truncated protein – TbTAX1^{Trunc} – are presented in Fig. S8B.

In this cell line, expression of *TbTAX-1^{RNAi}* – specifically targeting the full-length protein and not the truncated form – was inducible (Fig. 4A). Western blot analysis of fractionated samples (whole cells (WC), detergent-extracted cells or cytoskeletons (CSK), and the flagellum fraction (FG)), we localized the truncated TbTAX-1$^{Trunc}_{Ty1}$ protein (Fig. 4B). The

full-length TbTAX-1 protein was strongly associated with the axoneme, and was detected in the salt-extracted flagellum fraction. In contrast, the truncated TbTAX-1$^{Trunc}_{Ty1}$ form was detected neither in the flagellum nor in the cytoskeleton-associated fractions (Fig. 4B). These results were confirmed by IF on CSK (Fig. 4C). As expected, induction of *TbTAX-1^{RNAi}* led to decreased TbTAX-1 levels, but had no effect on TbTAX-1$^{Trunc}_{Ty1}$ (Fig. 4D). Cell growth was not affected (Fig. 4E), and the sedimentation phenotype was still observed (Fig. 4F). Thus, it appears that the N-terminal domain of TbTAX-1 is not involved in protein targeting and function, and cannot complement TbTAX-1 RNAi knock-down.

TbTTC29 and TAX-1 belong to the same protein complex; TbTTC29 expression depends on TbTAX-1

As indicated above, in IF analyses of spermatozoa from individuals bearing a mutated ZYMND12, proteins CFAP70, WDR66, TTC29, and SPAG6 were undetected. To further study associations between these proteins, we generated *T. brucei* TbTAX-1$_{HA}$/ *TbTAX-1^{RNAi}* background cell lines expressing their respective orthologs i.e., TbCFAP70$_{Ty1}$ (Tb927.10.2380), TbWDR66$_{Ty1}$ (Tb927.3.1670), TbTTC29$_{Ty1}$ (Tb927.3.1990), and $_{Ty1}$TbPF16/SPAG6 (Tb927.1.2670).

Western blotting revealed that CFAP70, WDR66 and SPAG6 were tightly associated with the flagellum fraction (Fig. S10A). However, none of these proteins was pulled down with Tb-TAX1 upon co-IP with the anti-Ty1 antibody (Fig. S10B). Furthermore, RNAi knock-down of TbTAX-1 expression did not alter their overall levels (Fig. S10C). The lack of direct interaction between TbTAX-1 and these three proteins was further confirmed by ultrastructure expansion microscopy IF (Gambarotto et al., 2019; Kalichava and Ochsenreiter, n.d.), which provided no evidence of colocalization (Fig. S10D).

In contrast, decreased TbTAX-1 levels were associated with decreased TbTTC29 expression, and *vice versa* according to western blot quantification (Fig. 5A and 6B). By IF, TbTAX-1 was also observed to co-localize with TbTTC29 on the axoneme (Fig. 5C). However, analysis of ultrastructure expansion microscopy (U-ExM) and confocal microscopy intensity peaks revealed the colocalization to be incomplete (Fig. 5D). Nevertheless, IP of TbTTC29$_{Ty1}$ from a TbTTC29$_{Ty1}$/TbTAX-1$_{HA}$ cell line pulled down TbTAX-1$_{HA}$ and *vice versa* (Fig. 5E). These results suggest that TbTAX-1 and TbTTC29 are part of the same protein complex.

The co-immunoprecipitated proteins were further analyzed by mass spectrometry. Comparative analysis of the significant hits in each co-IP (anti-Ty1 and anti-HA) (enrichment fold ≥2) identified two additional proteins enriched in both IPs: Tb927.11.3880 – a flagellar actin-like protein (Ersfeld and Gull, 2001) – and Tb927.11.8160 – a putative inner arm dynein heavy chain protein belonging to the IAD-4 protein family – (data summarized in Table S1). Tb927.11.8160 is potentially involved in flagellum motility (Wickstead and Gull, 2007), it localizes along the *T. brucei* axoneme according to the TrypTag genome-wide protein localization resource (http://tryptag.org/) (Dean et al., 2017). Significantly, BlastP searches of mammalian genomes for Tb927.11.8160 orthologs identified DNAH1 (Protein ID: XP_828890.1).

DNAH1 and DNALI1 both interact with TTC29 in mouse

In a recent human study, we showed that the presence of bi-allelic *TTC29* variants induces a MMAF phenotype and male infertility (Lorès et al., 2019). By CRISPR/Cas9 mutagenesis and RNAi silencing, we demonstrated that the orthologous TTC29 proteins in mouse and in *Trypanosoma brucei*, respectively, also constitute flagellar proteins that are

required for proper flagellum beating, indicating an evolutionarily-conserved function for TTC29 (Lorès et al., 2019).

Here, we took advantage of the availability of the mutant mouse model to further decipher the protein complexes associated with TTC29 function within the flagella. We performed comparative analyses of co-immunoprecipitations of testis protein extracts from WT mice using TTC29-specific antibodies, and from two previously generated TTC29 KO mouse lines lacking the TTC29 protein (*Ttc29*$^{-/-}$ L5 and L7) (Lorès et al., 2019). Mass spectrometry analyses of four independent experimental replicates for each mouse line identified a set of 124 proteins specifically immunoprecipitated in WT testes.

These proteins were further examined to identify TTC29 binding proteins (Table S2). Filtering of immunoprecipitated proteins based on peptide number and replicate constancy identified DNAH1 and DNALI1, in addition to TTC29, as the only proteins that were co-immunoprecipitated with a significant number of peptides in all four experimental replicates. In our previous study, DNAH1 and DNALI1 were detected at equal levels in flagella purified from WT and *Ttc29*$^{-/-}$ KO mice (Lorès et al., 2019). Therefore, we considered DNAH1 and DNALI1 to be authentic protein partners of TTC29 in sperm flagella, in line with data obtained with *Trypanosoma brucei*. Thus, our data indicate that ZMYND12 interacts with DNAH1 and DNALI1, two established components of the axonemal IDA.

DISCUSSION

The results presented here show that the presence of bi-allelic *ZMYND12* variants induces a typical MMAF phenotype in humans, suggesting that this gene is necessary for sperm flagellum structure and function. ZMYND12 is a previously uncharacterized MYND-domain-containing zinc finger protein, we therefore explored its localization and function using a recognized model: the flagellated protozoan *Trypanosoma*. This model is widely used to

investigate flagellum biogenesis and the function of flagellar proteins. In addition to having a very similar axonemal organization and composition to human flagellum, *Trypanosoma* has numerous advantages for functional studies, and is very useful for reverse genetics and biochemical or proteomics studies (Vincensini et al., 2011).

We first confirmed that ZMYND12 is an axonemal protein, and then used RNAi experiments to confirm its critical role in flagellum function. ZMYND12 knock-down led to dramatic flagellar motility defects like those observed in human sperm (Fig. 3). In addition, a truncated form of TAX-1 protein lacking the TPR domain – mimicking the expected truncated ZMYND12 protein in MMAF individuals bearing the p.Arg145Ter variant – was not associated with the flagellum, and failed to rescue TAX-1 RNAi-induced motility defects (Fig. 4). These results clearly indicate that the TPR motif of ZMYND12 is critical for protein targeting and function in both human sperm and *Trypanosoma*. Other groups also previously reported a significant role for TPR proteins in sperm flagellar biogenesis and male infertility (W. Liu et al., 2019; Lorès et al., 2019). Indeed, TPR domains are known to be involved in protein-protein interaction and the assembly of multiprotein complexes (D'Andrea and Regan, 2003). We therefore decided to further explore the potential interactions between ZMYND12 and other axonemal proteins.

IF experiments in sperm cells from ZMYND12 individuals revealed severe ultrastructural defects dramatically affecting several components of the axoneme. More specifically, IDAs and the CSC were severely disorganized, as shown by the total absence of DNAH1, WDR66 and DNALI1 immunostaining (Fig. 2A, 2B and S4B). Intriguingly, TTC29 and CFAP70 were also absent from sperm cells from individuals bearing ZMYND12 mutations (Fig. 2C and 2D). These observations suggest some functional or physical interaction between these proteins. However, the exact function and location of TTC29 and CFAP70 remain unclear. In *Chlamydomonas*, TTC29 has been suggested to be a component of IDAs (Yamamoto et al.,

2008), but this protein was also reported to possibly contribute to the IFT machinery (Brooks, 2014; Lorès et al., 2019). For CFAP70, functional studies in *Chlamydomonas* demonstrated that the protein localized at the base of the ODA, where it could regulate ODA activity (Shamoto et al., 2018). In *T. brucei*, we screened the axonemal proteins WDR66, CFAP70, SPAG6, and TTC29 to test their interaction with the ZMYND12 homolog. Our results indicated that TbTAX-1 only interacts with TbTTC29, and that the two proteins are part of the same axonemal complex (Fig. 5A and 5B). This interaction was confirmed by ultrastructure expansion microscopy and confocal microscopy (Fig. 5C and 5D). A third member of the complex – Tb927.11.8160, the ortholog of human DNAH1 – was subsequently identified by comparative proteomics analysis of co-immunoprecipitated proteins (Fig. 5E and Table S1). These results were further confirmed using the *Ttc29*-null mouse model previously generated in our laboratory (Table S2). All of these results are consistent with previous studies in *Chlamydomonas* suggesting that p38 (ZMYND12 ortholog) and p44 (TTC29 ortholog) interact and play a role in IDAd docking on the axoneme (Yamamoto et al., 2008). Interestingly, the axonemal IDAd in *Chlamydomona*s is composed of the DHC2 heavy chain and the p28 light chain, orthologs of human DNAH1 and DNALI1, respectively. Moreover, the recent human reference interactome map obtained by high-throughput two-hybrid screening (Luck et al., 2020) also supports direct protein-protein interaction between ZMYND12 and TTC29. Our results thus formally demonstrate that ZMYND12 interacts with TTC29 within the axonemal complex, in association with DNAH1 and inner dynein arms. DNAH1 is directly connected through an arc-like structure (King, 2013) to the base of radial spoke 3 (RS3), which is anchored to the axoneme by the CSC (Dymek et al., 2011). In humans and *Trypanosoma*, the absence of ZMYND12 in the flagellum probably destabilizes this axonemal complex, and consequently alters the stability of the RS3 base-docked IDAs including DNAH1, the CSC and RS. Each of these defects leads to severe axonemal disorganization, and a MMAF sperm phenotype. Our

team previously reported deleterious variants of *TTC29* and *DNAH1* associated with a MMAF phenotype. The flagellar defects caused by these variants are similar to those observed in sperm from individuals with *ZMYND12* defects (Ben Khelifa et al., 2014; C. Liu et al., 2019; Lorès et al., 2019). The results presented here thus contribute to elucidating the physical and functional associations between ZMYND12, TTC29 and DNAH1 in the axoneme, and emphasize the key role played by this triumvirate in maintaining the structure and function of the sperm flagellum.

Adding the three ZMYND12-mutated individuals to the 83 individuals previously identified with variants in known MMAF-related genes in our cohort of 167 individuals, we now have a diagnostic efficiency of 51.4% (86/167). This figure demonstrates the efficiency and the clinical utility of WES for the investigation of the genetic causes and pathophysiology of MMAF syndrome. Among the variants identified, we found the same *ZMYND12* nonsense variant c.433C>T; p.(Arg145Ter) in three unrelated individuals from diverse geographical origins (*i.e.*, Tunisia, China), suggesting that the Arg145 residue may constitute a mutational hotspot. Importantly, as previously reported (Kherraf et al., 2018), we confirmed that WES can detect small pathogenic exon deletions. These events may constitute a recurrent disease mechanism in MMAF, and should therefore be systematically explored. Despite these significant advances, the genetic cause of MMAF remains unknown for about half the individuals affected, due to the high genetic heterogeneity of the disorder. To improve the diagnostic rate, more powerful techniques such as whole-genome sequencing may now be envisaged for MMAF patients for whom WES fails to provide results (Meienberg et al., 2016).

The results presented here demonstrate that the combined use of exome sequencing and the *Trypanosoma* model can efficiently reveal new genes responsible for a MMAF phenotype in human and decipher how they affect sperm flagellum architecture and function. Overall, our strategy identified bi-allelic variants in *ZMYND12* associated with severe flagellum malformations resulting in asthenoteratozoospermia and primary male infertility. In conclusion,

our work with human sperm and the flagellated protist *T. brucei* demonstrated that ZMYND12 is part of the same axonemal complex as TTC29 and DNAH1, and plays a critical role in flagellum function and assembly.

MATERIALS AND METHODS

Study participants

WES data from a previously-established cohort of 167 MMAF individuals were analyzed (Coutton et al., 2019). All individuals presented a typical MMAF phenotype characterized by severe asthenozoospermia (total sperm motility below 10%), with >5% of the spermatozoa displaying at least three of the following flagellar abnormalities: short, absent, coiled, bent or irregular flagella (Coutton et al., 2019). All individuals had a normal somatic karyotype (46,XY) with normal bilateral testicular size, hormone levels, and secondary sexual characteristics. Sperm were analyzed in the source laboratories during routine biological examination of the individuals according to World Health Organization (WHO) guidelines (Wang et al., 2014). An additional Chinese individual was included in the study from a familial case. This individual was enrolled from the Human Sperm Bank of West China Second University Hospital of Sichuan University; he presented with severe asthenoteratozoospermia and a typical MMAF phenotype. WES analysis for this subject was performed as described in the previous report (Liu et al., 2021). Sperm morphology was assessed following Papanicolaou staining (Fig. 1A). Detailed semen parameters of the four individuals carrying *ZMYND12* mutations (*ZMYND12*$_{1\text{-}4}$) are presented in Table 1. Sperm samples for additional phenotypic characterization were obtained from *ZMYND12*$_{3}$. Written informed consent was obtained from all individuals participating in the study, and institutional approval was given by the local medical ethics committee (CHU Grenoble Alpes institutional review board). Samples were stored in the Fertithèque collection registered with the French Ministry of health (DC-2015-2580) and the French Data Protection Authority (DR-2016-392).

Sanger sequencing

ZMYND12 single nucleotide variants identified by exome sequencing were validated by Sanger sequencing as previously described (Coutton et al., 2019). PCR primers and protocols used for each individual are listed in the Table S3.

MLPA analysis

Deletion of exons 6-8 identified in individual ZMYND12_2 by exome sequencing was confirmed by custom MLPA analysis, according to our previously described method (Coutton et al., 2012). The MLPA probes were designed, and the MLPA reaction was performed according to the recommendations set out in the MRC-Holland synthetic protocol (www.mlpa.com). Data analysis was also performed in line with this protocol. For this study, three synthetic MLPA probes specific for exons 5, 6 and 8 of *ZMYND12* were designed. MLPA probes are listed in the Table S4.

Quantitative real-time RT-PCR (RT-qPCR) analysis

RT-qPCR experiments were performed as previously described (Coutton et al., 2019) with cDNAs extracted from various human tissues purchased from Life Technologies®. A panel of 10 organs was used for experiments: testis, brain, trachea, lung, kidney, liver, skeletal muscle, pancreas, placenta, and heart. Human RT-qPCR data were normalized relative to the two reference housekeeping genes *RPL6 and RPL27* by the $-\Delta\Delta C_t$ method (Livak and Schmittgen, 2001). Primer sequences and RT-qPCR conditions are indicated in Table S5. Relative expression of *ZMYND12* transcripts was compared in several organs, and statistical analysis involved a two-tailed *t*-test (Prism 4.0 software; GraphPad, San Diego, CA). A P-value ≤ 0.05 was considered significant.

Immunostaining in human sperm cells

Immunofluorescence (IF) experiments were performed on sperm cells from control individuals, from individual ZMYND12_3 – carrier of the nonsense variant c.103C>T – and from a previously-reported MMAF individual – carrier of the *TTC29* splicing variant c.1761+1G>A (Lorès et al., 2019). For each MMAF individual, 200 sperm cells were analyzed by two experienced operators, and the IF staining intensity and patterns were compared to those obtained from fertile control individuals. Sperm cells were fixed in phosphate-buffered saline (PBS)/4% paraformaldehyde for 1 min at room temperature. After washing in 1 mL PBS, the sperm suspension was spotted onto 0.1% poly L-lysine pre-coated slides (Thermo Scientific). After attachment, sperm were permeabilized with 0.1% (v/v) Triton X-100–DPBS (Triton X-100; Sigma-Aldrich) for 5 min at RT. Slides were then blocked by applying 5% normal serum–DPBS (normal goat or donkey serum; GIBCO, Invitrogen) before incubating overnight at 4 °C with the primary antibody. The following primary antibodies were used: ZMYND12, DNAI1, DNALI1, DNAH1, DNAH8, DNAH17, RSPH1, SPAG6, GAS8, CFAP70, WDR66 (also known as CFAP251), TTC29, AKAP4, and acetylated-α-tubulin. The primary antibody references and dilutions are fully detailed in Table S6. Slides were washed with 0.1% (v/v) Tween 20–DPBS before incubating for 1 h at room temperature with secondary antibodies. Highly cross-adsorbed secondary antibodies (Dylight 488 and Dylight 549, 1:1000) were purchased from Jackson Immunoresearch®. Experimental controls were treated similarly, but omitting the primary antibodies. Samples were counterstained with DAPI and mounted with DAKO mounting media (Life Technology). Fluorescence images were captured with a confocal microscope (Zeiss LSM 710).

***Trypanosoma brucei* cell lines, culture and transfection**

The trypanosome cell lines used in this study are derived from the procyclic parental form, *T. brucei* SmOxP427(Sunter, 2016). These cells co-express the T7 RNA polymerase and

the tetracycline repressor and were grown and transfected as previously described (Kherraf et al., 2018). When required, the culture medium was supplemented with puromycin (1 µg/mL), neomycin (10 µg/mL), phleomycin (5 µg/mL), or hygromycin (25 µg/mL). Cells were transfected using an AMAXA electroporator (Lonza) as previously described (Schumann Burkard et al., 2011). *TbTAX-1* RNA interference was induced with tetracycline (10 µg/mL).

Tagged proteins were obtained from SmOxP427 cells, by inserting epitope-tagged transgenes at the endogenous locus. Transgenes were N-terminally or C-terminally tagged with 10myc, 10Ty1, or 10HA tags using the pPOTv7 vector series, as previously described (Dean et al., 2015; Kherraf et al., 2018). For RNAi$^{TbTAX\text{-}1}$ knock-down, bp 219-667 were cloned between the *XhoI* and *XbaI* sites of p2T7tiB (LaCount et al., 2002) and the linearized vector was transfected into endogenously-tagged TbTAX-1-background cell lines. To target the full-length *TbTAX-1* and not the shorter form, similar cloning was performed with bp 493-917. The TbTTC29$_{Ty1}$ RNAi cell line is described elsewhere (Lorès et al., 2019).

Co-immunoprecipitation and Mass spectrometry on *Trypanosoma* cells

In a 15-mL polycarbonate tube, 2.10^8 cells expressing the different tagged proteins were washed in PBS and incubated for 5 min at RT in 1 mL of immunoprecipitation buffer for cell lysis (IP buffer; 25 mM Tris-HCl pH 7.4, 100 mM NaCl, 0.25% Nonidet P-40 (Igepal), 1 mM DTT, protease inhibitor cocktail, and 1 unit of nuclease) (Pierce). Lysis was completed by sonication (5x 30 s ON/30 s OFF) in a Bioruptor sonication system. Cell lysates were clarified by centrifugation (10 min, 16,000 x g, 4 °C) and split into two samples each. One was incubated with 3 µL of anti-Ty1 and the other with 2 µL of mouse anti-HA for 1 h at 4 °C on a rotating wheel. Protein-G Dynabead (Invitrogen 10003D) slurry (40 µL) was washed in IP buffer and incubated with the samples for 1 h at 4 °C. After washing three times in IP buffer, beads were resuspended in 40 µL sample buffer and boiled before loading 20 µL on SDS-PAGE.

For mass spectrometry analyses, $1.8x10^9$ cells were washed in PBS, resuspended in 2 mL of immunoprecipitation buffer without DTT and processed as described above. Antibodies used were: mouse anti-HA (10 µL) and anti-TY1 (15 µL). Complex precipitation was achieved by adding 200 µL of Protein-G Dynabead slurry. After washing three times in IP buffer, beads were transferred to new tubes and washed 3x in PBS before storing dry at -20 °C.

Protein-G Dynabeads were resuspended in Laemmli buffer and boiled. Supernatants were loaded on a 10% acrylamide SDS-PAGE gel, and proteins were revealed by Colloidal Blue staining. Sample preparation and protein digestion by trypsin were performed as previously described (Allmann et al., 2014). NanoLC-tandem mass spectrometry (MS/MS) analyses were performed using an Ultimate 3000 RSLC Nano-UPHLC system (Thermo Scientific, USA) coupled to a nanospray Orbitrap Fusion™ Lumos™ Tribrid™ Mass Spectrometer (Thermo Fisher Scientific, California, USA). Each peptide extract was loaded on a 300 µm ID x 5-mm PepMap C18 pre-column (Thermo Scientific, USA) at a flow rate of 10 µL/min. After a 3-min desalting step, peptides were separated on a 50-cm EasySpray column (75 µm ID, 2 µm C18 beads, 100 Å pore size; ES903, Thermo Fisher Scientific) by applying a 4-40% linear gradient of solvent B (0.1% formic acid in 80% ACN) over 48 min. The flow rate for separation was set to 300 nL/min. The mass spectrometer was operated in positive ion mode at a 2.0 kV needle voltage. Data were acquired using Xcalibur 4.4 software in data-dependent mode. MS scans (m/z 375-1500) were recorded at a resolution of R = 120,000 (@ m/z 200) and an Automated Gain Control (AGC) target of $4×10^5$ ions collected within 50 ms was applied along with a top speed duty cycle of up to 3 seconds for MS/MS acquisition. Precursor ions (2 to 7 charge states) were isolated in the quadrupole within a mass window of 1.6 Th, and fragmented by Higher energy Collisional Dissociation (HCD), applying 28% normalized collision energy. MS/MS data were acquired in the Orbitrap cell at a resolution of R=30000 (m/z 200), a standard AGC target and a maximum injection time in automatic mode. A 60-s

exclusion window was applied to previously selected precursors. Proteome Discoverer 2.5 was used to identify proteins and perform Label-Free Quantification (LFQ). Proteins were identified in batch mode using MS Amanda 2.0, Sequest HT and Mascot 2.5 algorithms, with searches performed against a *Trypanosoma brucei brucei* TREU927 protein database (9,788 entries, release 57, https://tritrypdb.org/ website). Up to two missed trypsin cleavages were allowed. Mass tolerances in MS and MS/MS were set to 10 ppm and 0.02 Da, respectively. Oxidation (M) and acetylation (K) were included as dynamic modifications, and carbamidomethylation (C) as a static modification. Peptides were validated using the Percolator algorithm (Käll et al., 2007), retaining only "high confidence" peptides, corresponding to a 1% false discovery rate at the peptide level. The minora feature-detector node (LFQ) was used along with the feature-mapper and precursor ion quantifier. The following quantification parameters were applied: (1) Unique peptides (2) Precursor abundance based on intensity (3) No normalization (4) Protein abundance calculation: summed abundances (5) Protein ratio calculation: pairwise ratios (6) Imputation mode: Low abundance resampling and (7) Hypothesis test: t-test (background-based). For master proteins, quantitative data were considered based on a minimum of two unique peptides, a fold-change greater than 2 and a Benjamini-Hochberg-corrected p-value for the FDR of less than 0.05. Mass spectrometry proteomics data have been deposited to the ProteomeXchange Consortium *via* the PRIDE partner repository (Deutsch et al., 2020), under dataset identifier PXD039470.

Immunofluorescence on *Trypanosoma* cells

Cells were harvested, washed, and processed for immunolabelling on methanol-fixed detergent-extracted cells (cytoskeleton, CSK) as described in (Albisetti et al., 2017). The antibodies used and their dilutions are listed in Table S7. Images were acquired on a Zeiss Imager Z1 microscope, using a Photometrics Coolsnap HQ2 camera, with a 100x Zeiss objective (NA 1.4) using Metamorph software (Molecular Devices), and processed with ImageJ

(NIH).

Ultrastructure expansion microscopy on *Trypanosoma* cells

The U-ExM protocol has been adapted and optimized for use on trypanosomes, as described (Gambarotto et al., 2021). Protocol details can be found online at https://doi.org/10.17504/protocols.io.bvwqn7dw (Casas et al., 2022). Images were acquired on a Zeiss AxioImager Z1 using a 63x (1.4 NA) objective, or at the Bordeaux Imaging Center with a Leica TCS SP5 on an upright stand DM6000 (Leica Microsystems, Mannheim, Germany), fitted with a HCX Plan Apo CS 63X oil NA 1.40 objective. Images were processed and analyzed using ImageJ and Fiji software (Schindelin et al., 2012; Schneider et al., 2012).

***Trypanosoma* cells: sedimentation assays and video microscopy**

Sedimentation assays were performed as described (Dacheux et al., 2012). Briefly, cells were placed in cuvettes and incubated for 24 h without shaking. Optical density (OD_{600nm}) was measured before mixing (ODb, to detect "swimming" cells) and after mixing (ODa, to detect "swimming" plus "sedimenting" cells). The percentage of sedimented cells was calculated as 100-(ODb/ODa) x100 for the WT and RNAi cells. Sedimentation of RNAi cells was normalized relative to the tagged TbTAX-1 parental cell line. Video microscopy was carried out as described (Lorès et al., 2019). Briefly, PCF cells (WT cell and RNAi$^{TbTAX\text{-}1}$ cells 72 h after induction) were washed in PBS, and cell mobility was recorded by phase-contrast microscopy on a Zeiss AxioImager Z1, 40x lens (NA 1.3). A 28-s sequence of digital video was captured from separate regions and analyzed using Metamorph software (Molecular Devices) (speed x8). The positions of individual cells were plotted over 0.28-s intervals. The start and end positions of each cell were marked.

Transmission Electron Microscopy (TEM) on *Trypanosoma* cells

TEM blocks of Trypanosoma cells and thin sections were prepared as previously described (Albisetti et al., 2017). Thin sections were visualized on an FEI Tecnai 12 electron microscope. Images were captured on an ORIUS 1000 11M Pixel camera (resolution 3±5 nm) controlled by Digitalmicrograph, and processed using ImageJ (NIH).

Western blot analyses of *Trypanosoma* cells

Proteins from whole cells, detergent-extracted cytoskeletons and flagella, or co-IPs were separated on SDS-PAGE gels. Separated proteins were transferred by semi-dry transfer to PVDF and low-fluorescence PVDF membranes for further processing, as described (Albisetti et al., 2017). The antibodies used and their dilutions are listed in Table S7. For IP analysis, primary antibodies – anti-TY1 and rabbit anti-HA (GTX115044) – and fluorescent secondary antibodies – anti-mouse Starbright Blue 520 (Bio-Rad 12005867) and anti-rabbit Starbright Blue 700 (Bio-Rad 12004162) – were used.

Co-immunoprecipitation and mass spectrometry analysis on *Ttc29*$^{-/-}$ mouse testes

Testes from wild type and Ttc29-/- L5 and L7 mice (Lorès et al., 2019) were dissected in cold PBS; the albuginea was removed and the seminiferous tubules were dissociated and pelleted by brief centrifugation. Proteins from the pellets were extracted in 1 mL lysis buffer: 50 mM Tris-HCl, pH 8, 150 mM NaCl, 10 mM MgCl2, 0.5% NP40, and Complete protease inhibitor cocktail (Roche Applied science). Immunoprecipitation was performed on total-protein lysate using 1 µg of rabbit polyclonal TTC29 antibody (HPA061473, Sigma-Aldrich) and 15 µl of Protein A/G magnetics beads (Bio-Ademtec) according to the manufacturer's instructions. The experiment was replicated with four mice for each genotype.

Total immunoprecipitated proteins were recovered in 25 µL 100 mM Tris/HCl pH 8.5 containing 10 mM TCEP, 40 mM chloroacetamide and 1% sodium deoxycholate, by sonicating three times, and incubating for 5 min at 95 °C. An aliquot (20 µg) of protein lysate was diluted (1:1) in Tris 25 mM pH 8.5 in 10% Acetonitrile (ACN) and subjected to overnight trypsin

digestion with 0.4 µg of sequencing-grade bovine trypsin (Promega) at 37 °C. Deoxycholate was removed using liquid-liquid phase extraction after adding 50 µL of 1% TriFluoroacetic Acid (TFA) in ethyl-acetate. A six-layer home-made Stagetip with Empore Styrene- divinylbenzene - Reversed Phase Sulfonate (SDB RPS; 3M) disks was used. Eluted peptides were dried and re-solubilized in 2% TFA before preparing five fractions on hand-made Strong Cation eXchange (SCX) StageTips (Kulak et al., 2014). Fractions were analyzed on a system combining an U3000 RSLC nanochromatograph eluting into an Orbitrap Fusion mass spectrometer (both Thermo Scientific). Briefly: peptides from each SCX fraction were separated on a C18 reverse phase column (2 µm particle size, 100 Å pore size, 75 µm inner diameter, 25 cm length) with a 145-min linear gradient starting from 99% solvent A (0.1% formic acid in H_2O) and ending with 40% of solvent B (80% ACN and 0.085% formic acid in H_2O). The MS1 scans spanned 350-1500 m/z with an AGC target of 1.10^6 within a maximum ion injection time (MIIT) of 60 ms, at a resolution of 60,000. The precursor selection window was set to 1.6 m/z with quadrupole filtering. HCD Normalized Collision Energy was set to 30%, and the ion trap scan rate was set to "rapid" mode with AGC target 1.10^5 and 60 ms MIIT. Mass spectrometry data were analyzed using Maxquant (v.1.6.1.0)(Cox et al., 2014). The database used was a concatenation of human sequences from the Uniprot-Swissprot database (release 2017-05) and the Maxquant list of contaminant sequences. Cysteine carbamidomethylation was set as fixed modification, and acetylation of protein N-terminus and oxidation of methionine were set as variable modifications. Second peptide search and "match between runs" (MBR) options were allowed. Label-free protein quantification (LFQ) was performed using both unique and razor peptides, requiring at least two peptides per protein. The quality of raw quantitative data was evaluated using PTXQC software v. 0.92.3 (Bielow et al., 2016). Perseus software, version 1.6.2.3 (Tyanova et al., 2016) was used for statistical analysis and data comparison. Proteomics data obtained by mass spectrometry analysis were deposited to the

ProteomeXchange Consortium *via* the PRIDE partner repository (Deutsch et al., 2020) under dataset identifier PXD039854.

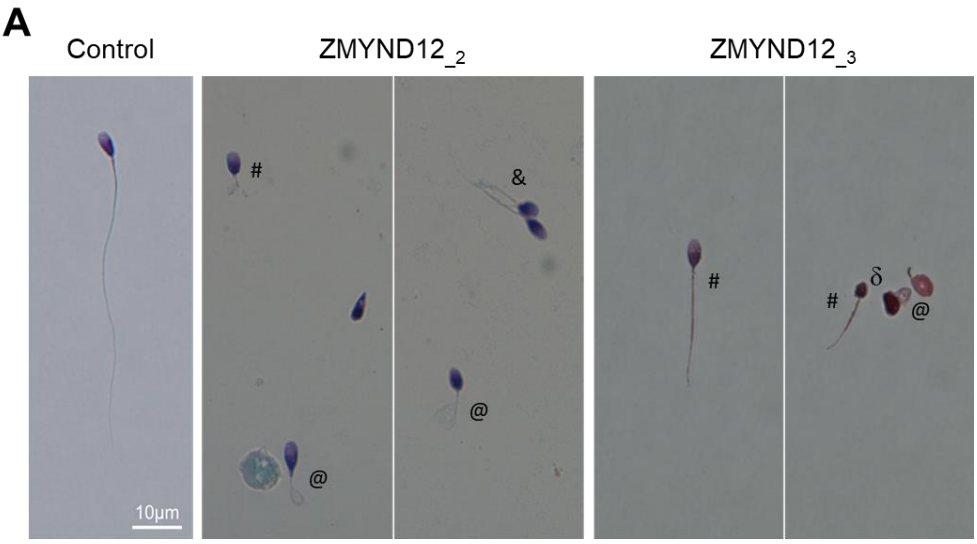

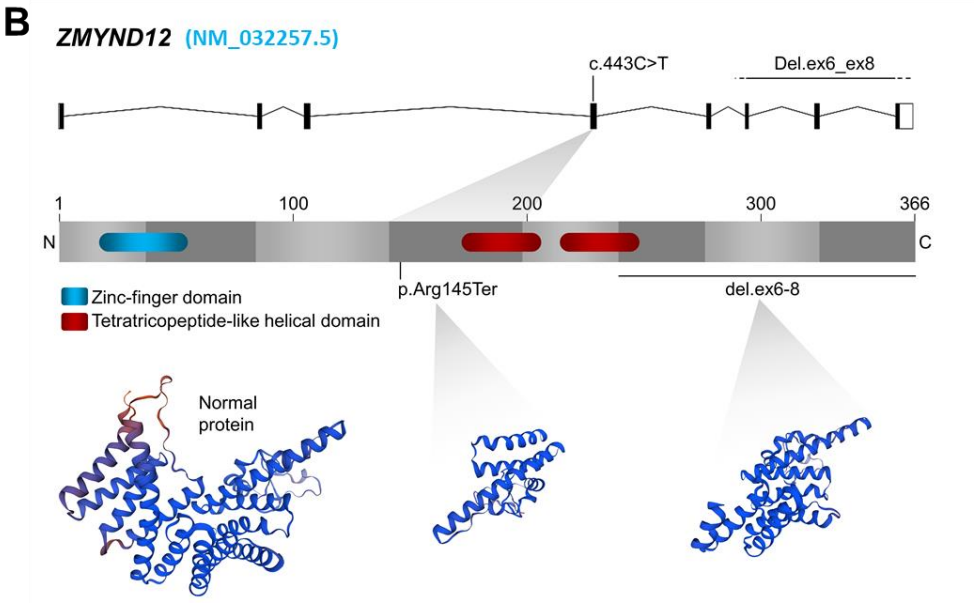

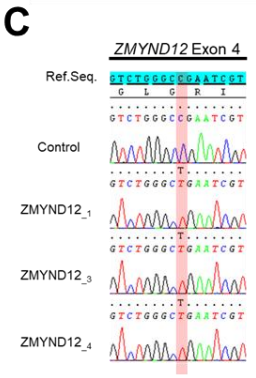

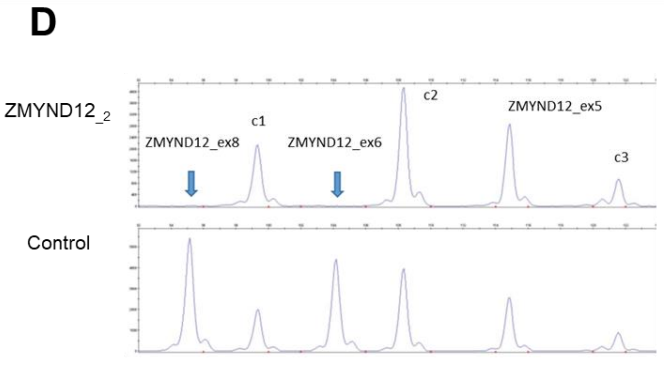

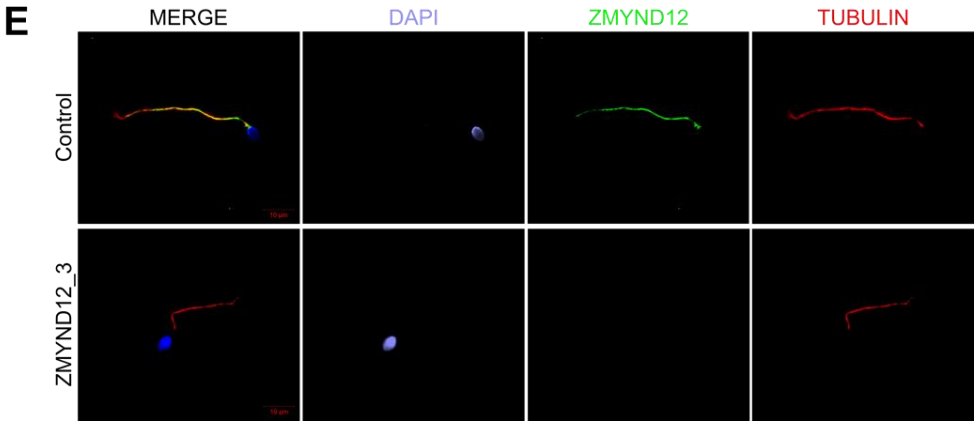

Fig. 1. Morphology of normal and *ZMYND12* mutant spermatozoa and variants identified in *ZMYND12* individuals. (**A**) Light microscopy analysis of spermatozoa from fertile control individuals and from individuals ZMYND12_2 and ZMYND12_3. Most spermatozoa from ZMYND12 individuals had short (#), coiled (@), or irregular caliber (&) flagella. Head malformations were also observed (δ). (**B**) Location of the variants identified within the *ZMYND12* gene (NM_032257.5) and protein according to UniprotKB (Q9H0C1). The blue box represents a Zinc Finger domain and the orange boxes represent TPR domains (tetratricopeptide repeat). (**C**) Sanger sequencing electropherograms indicating the homozygous state of the *c.433C>T* variant located in exon 4 in the three individuals ZMYND12_1,3 and 4. The substituted nucleotide is highlighted in red. Variants are annotated in line with HGVS recommendations. (**D**) Confirmation of *ZMYND12* exon deletion by MLPA. MLPA profiles obtained for control and ZMYND12_2 individuals. Each set contains three control probes for normalization purposes (c1-c3) and three *ZMYND12*-specific probes. Blue arrows indicate homozygous deletion of exons 6 and 8 in the *ZMYND12* gene. *ZMYND12* exon 5 is not included in the deletion. (**E**) Sperm cells from a fertile control individual and from individual ZMYND12_3 – carrier of the *c.433C>T* variant – were stained with anti-ZMYND12 (green) and anti-acetylated tubulin (red) antibodies. Sperm nuclear DNA was counterstained with DAPI (blue). In control sperm, ZMYND12 immunostaining was present along the whole length of the flagellum; no staining was observed in sperm cells from individual ZMYND12_3. Scale bars: 10 μm.

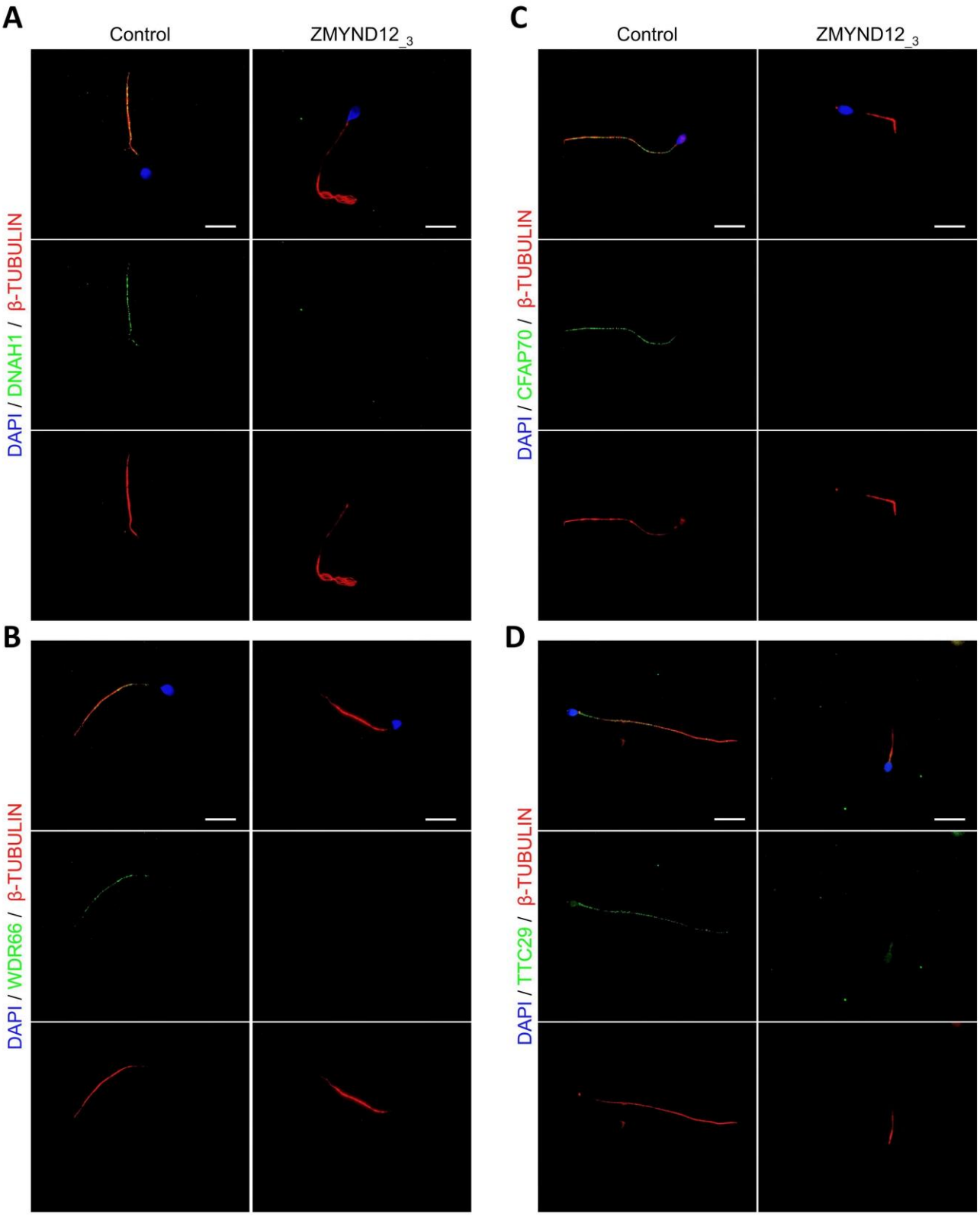

Fig. 2. Altered immunostaining for DNAH1, WDR66, CFAP70, and TTC29 in the presence of *ZMYND12* variants. Immunofluorescence experiments were performed using sperm cells from control individuals and from individual ZMYND12_3 carrying the nonsense variant *c.433C>T*. Although tubulin staining remained detectable, sperm cells from individual ZMYND12_3 showed no immunostaining for (**A**) DNAH1, (**B**) WDR66, (**C**) CFAP70 and (**D**) TTC29. Scale bars: 10 µm.

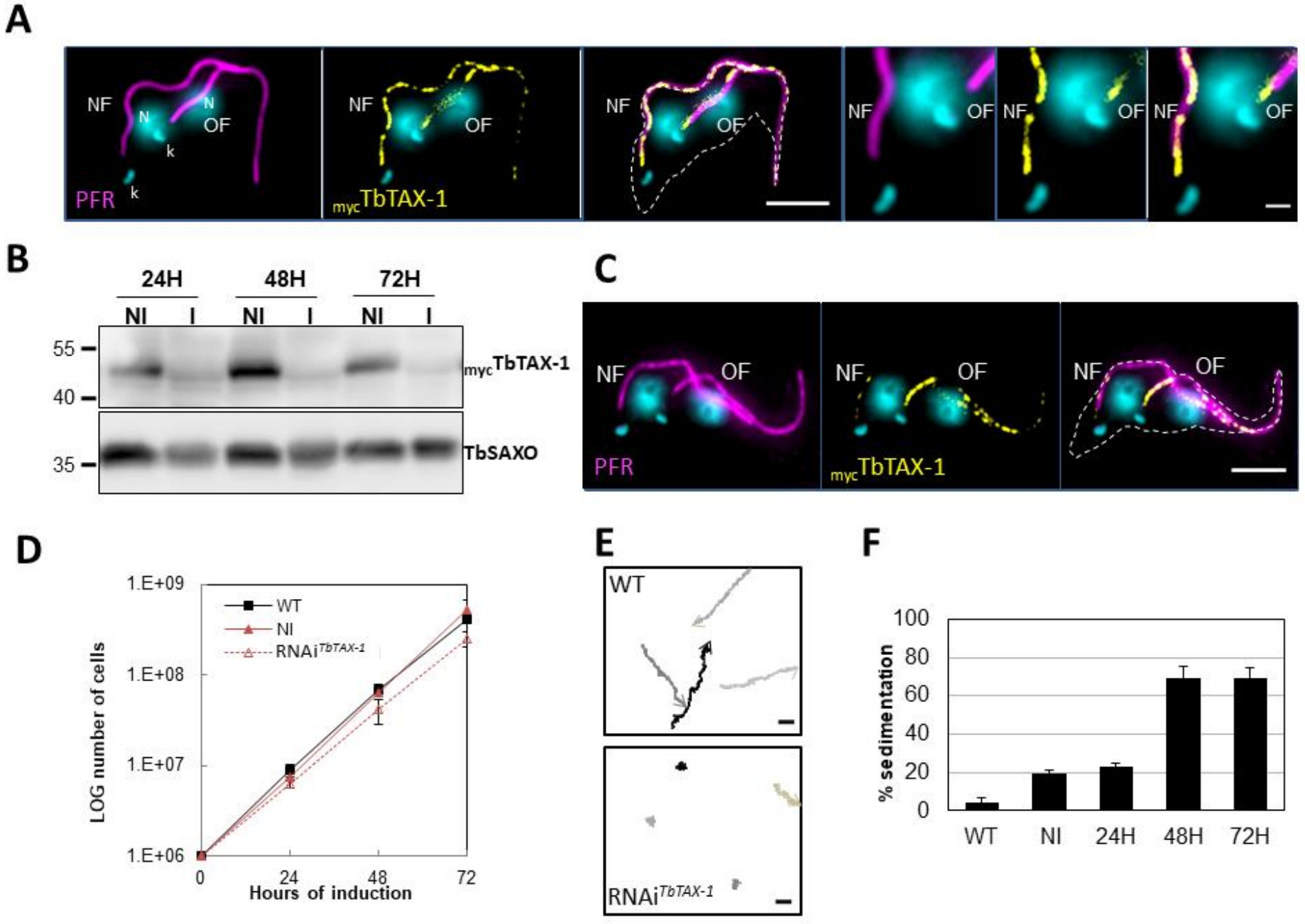
A
NF
N
N
OF
k
k
PFR
NF
OF
mycTbTAX-1
NF
OF
NF
OF
NF
OF
NF
OF
B
24H
48H
72H
NI
I
NI
I
NI
I
55
40
35
mycTbTAX-1
TbSAXO
C
NF
OF
PFR
NF
OF
mycTbTAX-1
NF
OF
D
1.E+09
1.E+08
1.E+07
1.E+06
LOG number of cells
WT
NI
RNAiTbTAX-1
0
24
48
72
Hours of induction
E
WT
RNAiTbTAX-1
F
100
80
60
40
20
0
% sedimentation
WT
NI
24H
48H
72H

Fig. 3. **TbTAX-1 is an axoneme-associated protein; its knock-down leads to flagellar motility defects.** (**A**) Representative image of a post-mitotic detergent-extracted cell immunolabelled with anti-PFR2 (magenta) staining the paraflagellar rod (a para-axonemal structure) and anti-myc (yellow) to reveal $_{myc}$TbTAX-1. The protein was detected on the axoneme in both the old flagellum (OF) and the new flagellum (NF). Immunolabelling indicated that the axonemal localization of $_{myc}$TbTAX-1 extended distally along the flagellum beyond the region labelled by PFR2 (see zoom). The mitochondrial genome (kinetoplast, k) and nuclei (N) were stained with DAPI. The outline of the cell body is indicated by the dashed white line. Scale bars: 5 μm in whole-cell images; 1 μm in zoomed images. (**B**) Anti-myc western blot analysis of RNAi$^{TbTAX-1}$ knock-down 24, 48, or 72 h post-induction. $_{myc}$TbTAX-1 protein levels were reduced in induced cells (I) compared to non-induced cells (NI); TbSAXO, a flagellum-specific protein, was used as loading control. (**C**) Representative image of a detergent-extracted post-mitotic cell after RNAi$^{TbTAX-1}$ induction, showing a strong decrease in $_{myc}$TbTAX-1 labeling in the NF compared to the OF. (**D**) Comparative *T. brucei* growth curves for wild-type (WT), non-induced (NI), and tetracycline-induced RNAi$^{TbTAX-1}$ cell lines at 0-, 24-, 48- and 72-hours post-induction. (**E**) Mobility tracking from video microscopy recordings of live cells: WT and RNAi$^{TbTAX-1}$ after induction for 72 h. The positions of individual cells are plotted at 0.28-s intervals; circles indicate start positions, arrowheads indicate end positions. A dramatic loss of progressive mobility was observed after TbTAX1 protein knock-down. Scale bars: 20 μm. (**F**) Sedimentation assays for *T. brucei* WT, non-induced (NI), and tetracycline-induced RNAi$^{TbTAX-1}$ at 24, 48, and 72 h post-induction. The percentage of cells sedimenting increased from 20 to 70% after depletion of the TbTAX-1 protein.

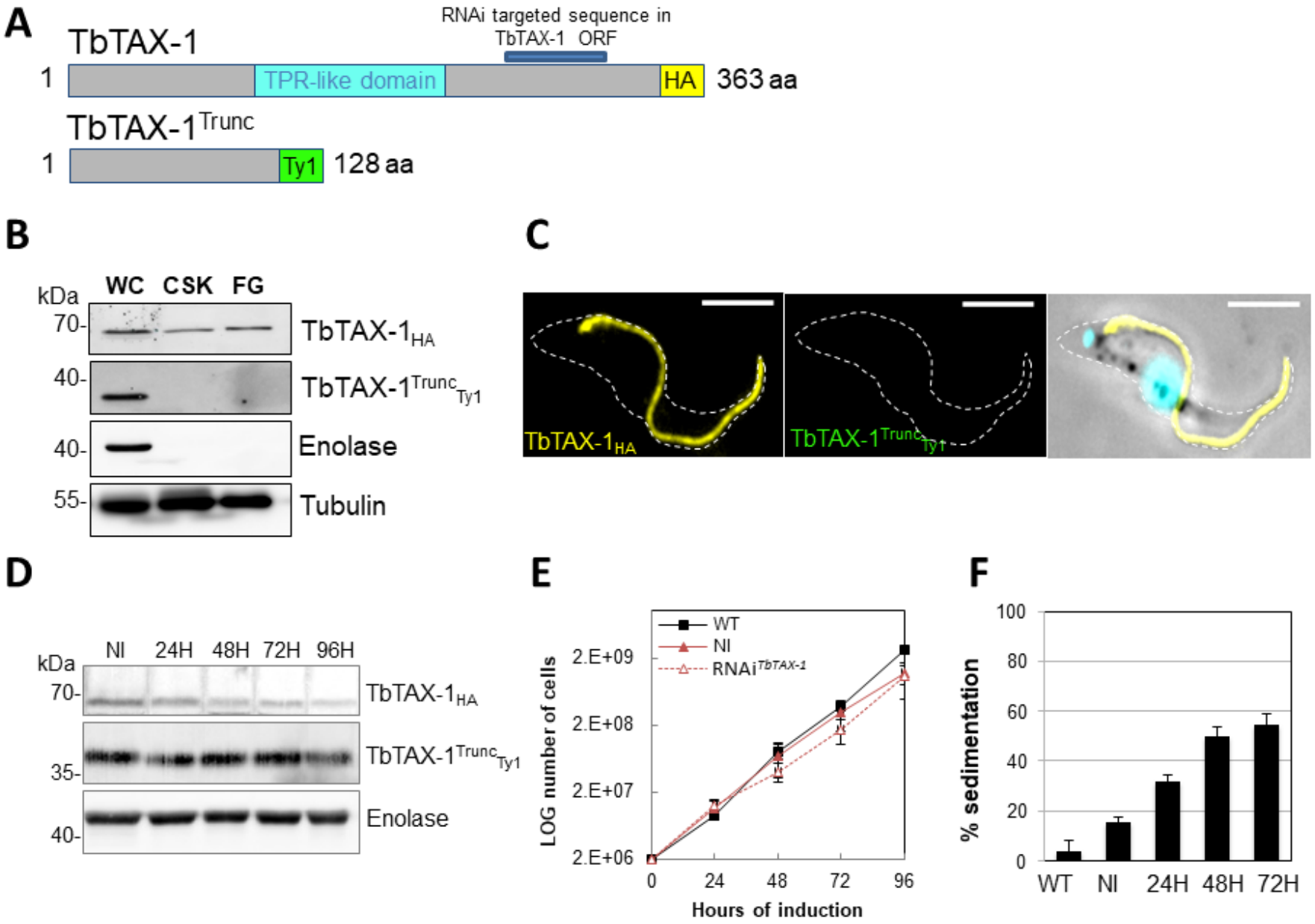
A
TbTAX-1
RNAi targeted sequence in TbTAX-1 ORF
1
TPR-like domain
HA
363 aa
TbTAX-1Trunc
1
Ty1
128 aa
B
kDa
WC CSK FG
70-
TbTAX-1HA
40-
TbTAX-1TruncTy1
40-
Enolase
55-
Tubulin
C
TbTAX-1HA
TbTAX-1TruncTy1
D
kDa
NI 24H 48H 72H 96H
70-
TbTAX-1HA
35-
TbTAX-1TruncTy1
40-
Enolase
E
LOG number of cells
2.E+09
2.E+08
2.E+07
2.E+06
WT
NI
RNAiTbTAX-1
0 24 48 72 96
Hours of induction
F
% sedimentation
100
80
60
40
20
0
WT NI 24H 48H 72H

Fig. 4. The truncated form of TbTAX-1 is not functional. (**A**) Schematic representation of full-length TbTAX-1 and its truncated form. The TPR-like domain is illustrated in light blue, and the targeted RNA interference sequence in dark blue. (**B**) Western blot analysis of subcellular fractions to determine localization of TbTAX-1_{HA} and its truncated form TbTAX-$1^{Trunc}{}_{Ty1}$. Enolase (cytoplasm) and tubulin (cytoskeleton) were used as loading controls. (**C**) Immunofluorescence-labeling of detergent-extracted cytoskeletons to detect TbTAX-1_{HA} (yellow) and TbTAX-$1^{Trunc}{}_{Ty1}$ (stained green, but not visible as the protein was eliminated during detergent extraction). Scale bars: 5 μm. (**D**) Western blot analysis of the impact of RNAi$^{TbTAX\text{-}1}$ expression on TbTAX-$1^{Trunc}{}_{Ty1}$ levels. Enolase was used as a loading control. (**E**) Growth curves of WT, non-induced (NI), and RNAi$^{TbTAX\text{-}1}$ induced cells expressing TbTAX-1_{HA} and TbTAX-$1^{Trunc}{}_{Ty1}$. (**F**) Sedimentation assays for *T. brucei* WT, non-induced (NI), and RNAi$^{TbTAX\text{-}1}$ induced cells at 24, 48, and 72 h.

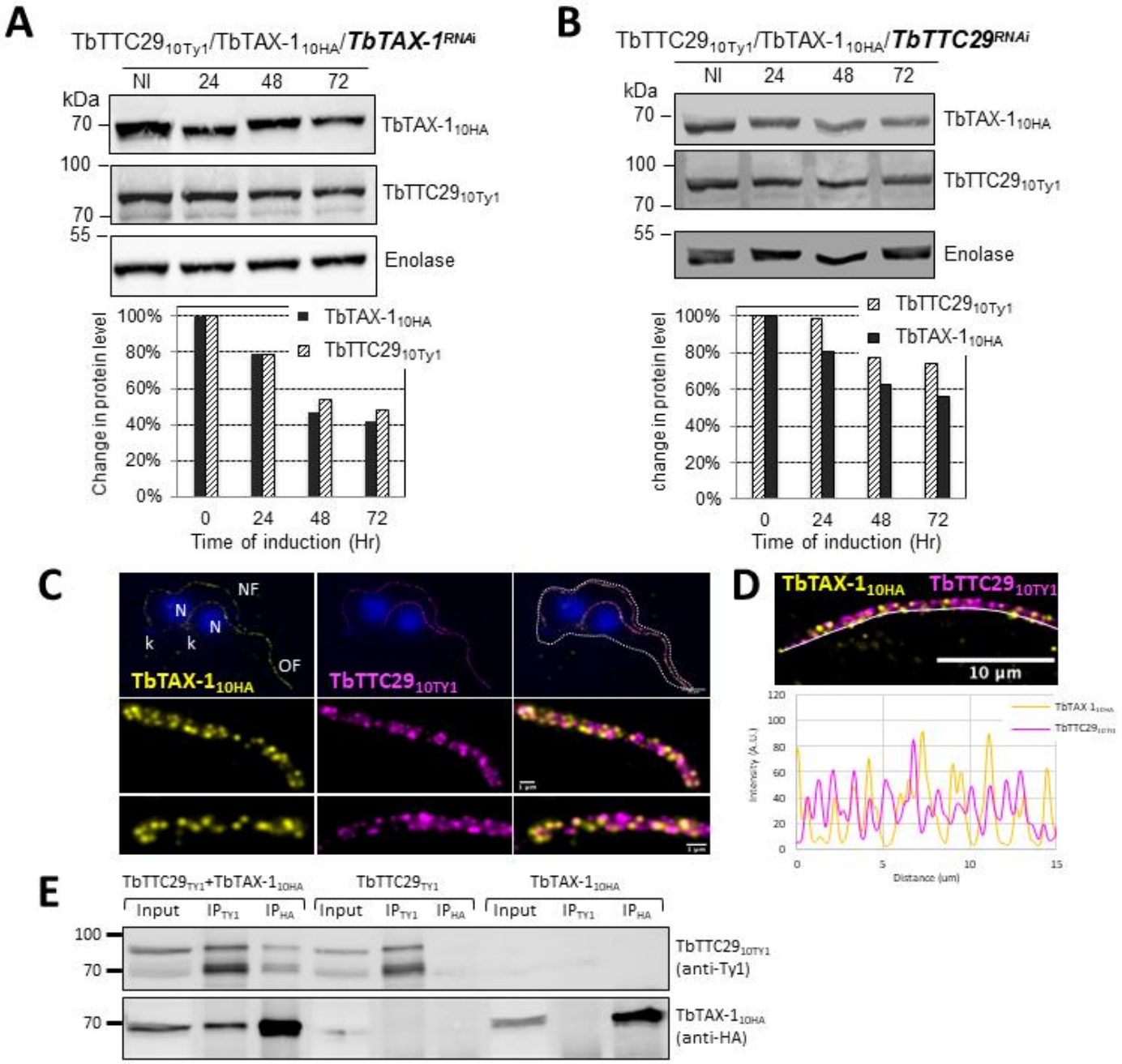
A
TbTTC29$_{10Ty1}$/TbTAX-1$_{10HA}$/*TbTAX-1^{RNAi}*
NI
24
48
72
kDa
70
100
70
55
TbTAX-1$_{10HA}$
TbTTC29$_{10Ty1}$
Enolase
Change in protein level
100%
80%
60%
40%
20%
0%
TbTAX-1$_{10HA}$
TbTTC29$_{10Ty1}$
0
24
48
72
Time of induction (Hr)
B
TbTTC29$_{10Ty1}$/TbTAX-1$_{10HA}$/*TbTTC29^{RNAi}*
NI
24
48
72
kDa
70
100
70
55
TbTAX-1$_{10HA}$
TbTTC29$_{10Ty1}$
Enolase
change in protein level
100%
80%
60%
40%
20%
0%
TbTTC29$_{10Ty1}$
TbTAX-1$_{10HA}$
0
24
48
72
Time of induction (Hr)
C
NF
N
N
k
k
OF
TbTAX-1$_{10HA}$
TbTTC29$_{10TY1}$
D
TbTAX-1$_{10HA}$
TbTTC29$_{10TY1}$
10 µm
120
100
80
60
40
20
0
Intensity (A.U.)
TbTAX 1$_{10HA}$
TbTTC29$_{10TY1}$
0
5
10
15
Distance (um)
E
TbTTC29$_{TY1}$+TbTAX-1$_{10HA}$
TbTTC29$_{TY1}$
TbTAX-1$_{10HA}$
Input
IP$_{TY1}$
IP$_{HA}$
Input
IP$_{TY1}$
IP$_{HA}$
Input
IP$_{TY1}$
IP$_{HA}$
100
70
70
TbTTC29$_{10TY1}$
(anti-Ty1)
TbTAX-1$_{10HA}$
(anti-HA)

Fig. 5. TbTAX-1 and TbTTC29 are part of the same protein complex. (**A**) Analysis of the impact of *TbTAX-1* RNAi on TbTTC29$_{Ty1}$ protein levels. Western blot (upper panel) and quantification (lower panel). (**B**) Analysis of the impact of *TbTTC29* RNAi induction on TbTAX-1$_{HA}$ protein levels. Western blot (upper panel) and quantification (lower panel). (**C**) U-ExM analysis of TbTAX-1$_{HA}$ (yellow) and TbTTC29$_{TY1}$ (purple) colocalization in a dividing cell with an old flagellum (OF) and a new flagellum (NF). Kinetoplast (k) and nuclei (N) were counterstained with Hoechst (blue). (**D**) Confocal image of U-ExM labelling of TbTAX-1$_{HA}$ (yellow) and TbTTC29$_{TY1}$ (magenta) (upper panel). Lower panel: profile plot along the white line showing overlapping intensity peaks for TbTAX-1 and TbTTC29, confirming true colocalization. (**E**) Anti-Ty1 (IP$_{Ty1}$) or anti-HA (IP$_{HA}$) co-immunoprecipitation assays in cell lines expressing both TbTAX-1$_{HA}$ and TbTTC29$_{Ty1}$, or TbTTC29$_{Ty1}$ alone or TbTAX-1$_{HA}$ alone to verify IP specificity. Proteins were detected simultaneously by western blotting using anti-Ty1 and anti-HA antibodies and fluorescent anti-mouse (detecting mouse anti-Ty1) and anti-rabbit (detecting rabbit anti-HA) secondary antibodies. IP assays on cell lines expressing only one or the other tagged protein did not pull down the other tagged protein.

Table 1. Detailed semen parameters in the four MMAF individuals harboring a *ZMYND12* variant.

***ZMYND12* mutated individuals**		**Semen parameters**															
Individuals	Homozygous *ZMYND12* variants	Sperm volume (mL)	Sperm concentration (10^6/mL)	Total motility 1 h	Vitality	Normal spermatozoa	Absent flagella	Short Flagella	Coiled Flagella	Bent Flagella	Flagella of irregular caliber	Tapered head	Thin head	Micro-cephalic	Macro-cephalic	Multiple heads	Abnormal base	Abnormal acrosomal region
ZMYND12_1	c.433C>T	2	6.5	4	70	0	35	48	10	0	34	22	2	2	4	6	20	80
ZMYND12_2	Del ex6-8	2.5	4.25	2	NA	0	NA	72	NA	NA	NA	NA	NA	NA	NA	NA	NA	NA
ZMYND12_3	c.433C>T	3	34	2	50	0	20	20	28	0	46	22	6	8	2	2	24	88
ZMYND12_4	c.433C>T	2.6	0.1	0	NA	NA	NA	70	NA	NA	NA	NA	NA	NA	NA	NA	NA	NA
Reference limits[a]		1.5 (1.4-1.7)	15 (12-16)	40 (38-42)	58 (55-63)	23 (20-26)	5 (4-6)	1 (0-2)	17 (15-19)	13 (11-15)	2 (1-3)	3 (2-4)	14 (12-16)	7 (5-9)	1 (0-2)	2 (1-3)	42 (39-45)	60 (57-63)

Values are percentages unless specified otherwise. NA: not available

[a] Reference limits (5th centiles and their 95% confidence intervals) according to World Health Organization (WHO) standards (Cooper et al., 2010) and the distribution range of morphologically normal spermatozoa observed in 926 fertile individuals (Auger et al., 2016).

REFERENCES AND NOTES

Albisetti A, Florimond C, Landrein N, Vidilaseris K, Eggenspieler M, Lesigang J, Dong G, Robinson DR, Bonhivers M. 2017. Interaction Between the Flagellar Pocket Collar and the Hook Complex via a Novel Microtubule-binding Protein in Trypanosoma brucei. *PLOS Pathog* **13**:e1006710. doi:10.1371/journal.ppat.1006710

Allmann S, Mazet M, Ziebart N, Bouyssou G, Fouillen L, Dupuy J-W, Bonneu M, Moreau P, Bringaud F, Boshart M. 2014. Triacylglycerol Storage in Lipid Droplets in Procyclic Trypanosoma brucei. *PLOS ONE* **9**:e114628. doi:10.1371/journal.pone.0114628

Arafah K, Lopez F, Cazin C, Kherraf Z-E, Tassistro V, Loundou A, Arnoult C, Thierry-Mieg N, Bulet P, Guichaoua M-R, Ray PF. 2021. Defect in the nuclear pore membrane glycoprotein 210-like gene is associated with extreme uncondensed sperm nuclear chromatin and male infertility: a case report. *Hum Reprod Oxf Engl* **36**:693–701. doi:10.1093/humrep/deaa329

Aslett M, Aurrecoechea C, Berriman M, Brestelli J, Brunk BP, Carrington M, Depledge DP, Fischer S, Gajria B, Gao X, Gardner MJ, Gingle A, Grant G, Harb OS, Heiges M, Hertz-Fowler C, Houston R, Innamorato F, Iodice J, Kissinger JC, Kraemer E, Li W, Logan FJ, Miller JA, Mitra S, Myler PJ, Nayak V, Pennington C, Phan I, Pinney DF, Ramasamy G, Rogers MB, Roos DS, Ross C, Sivam D, Smith DF, Srinivasamoorthy G, Stoeckert CJ, Subramanian S, Thibodeau R, Tivey A, Treatman C, Velarde G, Wang H. 2010. TriTrypDB: a functional genomic resource for the Trypanosomatidae. *Nucleic Acids Res* **38**:D457-462. doi:10.1093/nar/gkp851

Auger J, Jouannet P, Eustache F. 2016. Another look at human sperm morphology. *Hum Reprod Oxf Engl* **31**:10–23. doi:10.1093/humrep/dev251

Baron DM, Ralston KS, Kabututu ZP, Hill KL. 2007. Functional genomics in Trypanosoma brucei identifies evolutionarily conserved components of motile flagella. *J Cell Sci* **120**:478–91. doi:10.1242/jcs.03352

Ben Khelifa M, Coutton C, Zouari R, Karaouzène T, Rendu J, Bidart M, Yassine S, Pierre V, Delaroche J, Hennebicq S, Grunwald D, Escalier D, Pernet-Gallay K, Jouk P-S, Thierry-Mieg N, Touré A, Arnoult C, Ray PF. 2014. Mutations in DNAH1, which encodes an inner arm heavy chain dynein, lead to male infertility from multiple morphological abnormalities of the sperm flagella. *Am J Hum Genet* **94**:95–104. doi:10.1016/j.ajhg.2013.11.017

Bielow C, Mastrobuoni G, Kempa S. 2016. Proteomics Quality Control: Quality Control Software for MaxQuant Results. *J Proteome Res* **15**:777–787. doi:10.1021/acs.jproteome.5b00780

Blackburn K, Bustamante-Marin X, Yin W, Goshe MB, Ostrowski LE. 2017. Quantitative Proteomic Analysis of Human Airway Cilia Identifies Previously Uncharacterized Proteins of High Abundance. *J Proteome Res* **16**:1579–1592. doi:10.1021/acs.jproteome.6b00972

Broadhead Richard, Dawe HR, Farr H, Griffiths S, Hart SR, Portman N, Shaw MK, Ginger ML, Gaskell SJ, McKean PG, Gull K. 2006. Flagellar motility is required for the viability of the bloodstream trypanosome. *Nature* **440**:224–227. doi:10.1038/nature04541

Brookman JL, Stott AJ, Cheeseman PJ, Burns NR, Adams SE, Kingsman AJ, Gull K. 1995. An immunological analysis of Ty1 virus-like particle structure. *Virology* **207**:59–67. doi:10.1006/viro.1995.1051

Brooks ER. 2014. Control of intraflagellar transport : studies of the planar cell polarity effector Fuz, the small GTPase Rsg1, and the novel protein TTC29 (Thesis).

Casas E, Landrein N, Bonhivers M. 2022. Ultra Expansion microscopy protocol with improved setup for upright and inverted microscopes. *protocols.io*. https://www.protocols.io/view/ultra-expansion-microscopy-protocol-with-improved-bvwqn7dw

Cooper TG, Noonan E, von Eckardstein S, Auger J, Baker HWG, Behre HM, Haugen TB, Kruger T, Wang C, Mbizvo MT, Vogelsong KM. 2010. World Health Organization reference values for human semen characteristics. *Hum Reprod Update* **16**:231–245. doi:10.1093/humupd/dmp048

Coutton C, Escoffier J, Martinez G, Arnoult C, Ray PF. 2015. Teratozoospermia: spotlight on the main genetic actors in the human. *Hum Reprod Update* **21**:455–485. doi:10.1093/humupd/dmv020

Coutton C, Martinez G, Kherraf Z-E, Amiri-Yekta A, Boguenet M, Saut A, He X, Zhang F, Cristou-Kent M, Escoffier J, Bidart M, Satre V, Conne B, Fourati Ben Mustapha S, Halouani L, Marrakchi O, Makni M, Latrous H, Kharouf M, Pernet-Gallay K, Bonhivers M, Hennebicq S, Rives N, Dulioust E, Touré A, Gourabi H, Cao Y, Zouari R, Hosseini SH, Nef S, Thierry-Mieg N, Arnoult C, Ray PF. 2019. Bi-allelic Mutations in ARMC2 Lead to Severe Astheno-Teratozoospermia Due to Sperm Flagellum Malformations in Humans and Mice. *Am J Hum Genet* **104**:331–340. doi:10.1016/j.ajhg.2018.12.013

Coutton C, Vargas AS, Amiri-Yekta A, Kherraf Z-E, Ben Mustapha SF, Le Tanno P, Wambergue-Legrand C, Karaouzène T, Martinez G, Crouzy S, Daneshipour A, Hosseini SH, Mitchell V, Halouani L, Marrakchi O, Makni M, Latrous H, Kharouf M, Deleuze J-F, Boland A, Hennebicq S, Satre V, Jouk P-S, Thierry-Mieg N, Conne B, Dacheux D, Landrein N, Schmitt A, Stouvenel L, Lorès P, El Khouri E, Bottari SP, Fauré J, Wolf J-P, Pernet-Gallay K, Escoffier J, Gourabi H, Robinson DR, Nef S, Dulioust E, Zouari R, Bonhivers M, Touré A, Arnoult C, Ray PF. 2018. Mutations in CFAP43 and CFAP44 cause male infertility and flagellum defects in Trypanosoma and human. *Nat Commun* **9**:686. doi:10.1038/s41467-017-02792-7

Coutton C, Zouari R, Abada F, Ben Khelifa M, Merdassi G, Triki C, Escalier D, Hesters L, Mitchell V, Levy R, Sermondade N, Boitrelle F, Vialard F, Satre V, Hennebicq S, Jouk P-S, Arnoult C, Lunardi J, Ray PF. 2012. MLPA and sequence analysis of DPY19L2 reveals point mutations causing globozoospermia. *Hum Reprod Oxf Engl* **27**:2549–2558. doi:10.1093/humrep/des160

Cox J, Hein MY, Luber CA, Paron I, Nagaraj N, Mann M. 2014. Accurate proteome-wide label-free quantification by delayed normalization and maximal peptide ratio extraction, termed MaxLFQ. *Mol Cell Proteomics MCP* **13**:2513–2526. doi:10.1074/mcp.M113.031591

Crozier TWM, Tinti M, Wheeler RJ, Ly T, Ferguson MAJ, Lamond AI. 2018. Proteomic Analysis of the Cell Cycle of Procylic Form Trypanosoma brucei. *Mol Cell Proteomics MCP* **17**:1184–1195. doi:10.1074/mcp.RA118.000650

Dacheux D, Landrein N, Thonnus M, Gilbert G, Sahin A, Wodrich H, Robinson DR, Bonhivers M. 2012. A MAP6-Related Protein Is Present in Protozoa and Is Involved in Flagellum Motility. *PLoS One* **7**:e31344. doi:10.1371/journal.pone.0031344

D'Andrea LD, Regan L. 2003. TPR proteins: the versatile helix. *Trends Biochem Sci* **28**:655–662. doi:10.1016/j.tibs.2003.10.007

Darde TA, Lecluze E, Lardenois A, Stévant I, Alary N, Tüttelmann F, Collin O, Nef S, Jégou B, Rolland AD, Chalmel F. 2019. The ReproGenomics Viewer: a multi-omics and cross-species resource compatible with single-cell studies for the reproductive science community. *Bioinforma Oxf Engl* **35**:3133-3139. doi:10.1093/bioinformatics/btz047

Dean S, Moreira-Leite F, Varga V, Gull K. 2016. Cilium transition zone proteome reveals compartmentalization and differential dynamics of ciliopathy complexes. *Proc Natl Acad Sci U S A* **113**:E5135-5143. doi:10.1073/pnas.1604258113

Dean S, Sunter J, Wheeler RJ, Hodkinson I, Gluenz E, Gull K. 2015. A toolkit enabling efficient, scalable and reproducible gene tagging in trypanosomatids. *Open Biol* **5**:140197. doi:10.1098/rsob.140197

Dean S, Sunter JD, Wheeler RJ. 2017. TrypTag.org: A Trypanosome Genome-wide Protein Localisation Resource. *Trends Parasitol* **33**:80–82. doi:10.1016/j.pt.2016.10.009

Deutsch EW, Bandeira N, Sharma V, Perez-Riverol Y, Carver JJ, Kundu DJ, García-Seisdedos D, Jarnuczak AF, Hewapathirana S, Pullman BS, Wertz J, Sun Z, Kawano S, Okuda S, Watanabe Y, Hermjakob H, MacLean B, MacCoss MJ, Zhu Y, Ishihama Y, Vizcaíno JA. 2020. The ProteomeXchange consortium in 2020: enabling 'big data' approaches in proteomics. *Nucleic Acids Res* **48**:D1145–D1152. doi:10.1093/nar/gkz984

Dymek EE, Heuser T, Nicastro D, Smith EF. 2011. The CSC is required for complete radial spoke assembly and wild-type ciliary motility. *Mol Biol Cell* **22**:2520–2531. doi:10.1091/mbc.E11-03-0271

Ersfeld K, Gull K. 2001. Targeting of cytoskeletal proteins to the flagellum of Trypanosoma brucei. *J Cell Sci* **114**:141–148. doi:10.1242/jcs.114.1.141

Gambarotto D, Hamel V, Guichard P. 2021. Chapter 4 - Ultrastructure expansion microscopy (U-ExM) In: Guichard P, Hamel V, editors. Methods in Cell Biology, Expansion Microscopy for Cell Biology. Academic Press. pp. 57–81. doi:10.1016/bs.mcb.2020.05.006

Gambarotto D, Zwettler FU, Guennec ML, Schmidt-Cernohorska M, Fortun D, Borgers S, Heine J, Schloetel J-G, Reuss M, Unser M, Boyden ES, Sauer M, Hamel V, Guichard P. 2019. Imaging cellular ultrastructures using expansion microscopy (U-ExM). *Nat Methods* **16**:71–74. doi:10.1038/s41592-018-0238-1

Hannaert V, Albert M-A, Rigden DJ, da Silva Giotto MT, Thiemann O, Garratt RC, Van Roy J, Opperdoes FR, Michels PAM. 2003. Kinetic characterization, structure modelling studies and crystallization of Trypanosoma brucei enolase. *Eur J Biochem* **270**:3205–3213. doi:10.1046/j.1432-1033.2003.03692.x

Kalichava A, Ochsenreiter T. n.d. Ultrastructure expansion microscopy in Trypanosoma brucei. *Open Biol* **11**:210132. doi:10.1098/rsob.210132

Käll L, Canterbury JD, Weston J, Noble WS, MacCoss MJ. 2007. Semi-supervised learning for peptide identification from shotgun proteomics datasets. *Nat Methods* **4**:923–925. doi:10.1038/nmeth1113

Kherraf Z-E, Amiri-Yekta A, Dacheux D, Karaouzène T, Coutton C, Christou-Kent M, Martinez G, Landrein N, Le Tanno P, Fourati Ben Mustapha S, Halouani L, Marrakchi O, Makni M, Latrous H, Kharouf M, Pernet-Gallay K, Gourabi H, Robinson DR, Crouzy S, Blum M, Thierry-Mieg N, Touré A, Zouari R, Arnoult C, Bonhivers M, Ray PF. 2018. A Homozygous Ancestral SVA-Insertion-Mediated Deletion in WDR66 Induces Multiple Morphological Abnormalities of the Sperm Flagellum and Male Infertility. *Am J Hum Genet* **103**:400–412. doi:10.1016/j.ajhg.2018.07.014

Kim S, Scheffler K, Halpern AL, Bekritsky MA, Noh E, Källberg M, Chen X, Kim Y, Beyter D, Krusche P, Saunders CT. 2018. Strelka2: fast and accurate calling of germline and somatic variants. *Nat Methods* **15**:591–594. doi:10.1038/s41592-018-0051-x

King SM. 2013. A solid-state control system for dynein-based ciliary/flagellar motility. *J Cell Biol* **201**:173–175. doi:10.1083/jcb.201302077

Kulak NA, Pichler G, Paron I, Nagaraj N, Mann M. 2014. Minimal, encapsulated proteomic-sample processing applied to copy-number estimation in eukaryotic cells. *Nat Methods* **11**:319–324. doi:10.1038/nmeth.2834

LaCount DJ, Barrett B, Donelson JE. 2002. Trypanosoma brucei FLA1 is required for flagellum attachment and cytokinesis. *J Biol Chem* **277**:17580–8.

Liu C, He X, Liu W, Yang S, Wang L, Li W, Wu H, Tang S, Ni X, Wang J, Gao Y, Tian S, Zhang L, Cong J, Zhang Z, Tan Q, Zhang J, Li H, Zhong Y, Lv M, Li J, Jin L, Cao Y, Zhang F. 2019. Bi-allelic Mutations in TTC29 Cause Male Subfertility with Asthenoteratospermia in Humans and Mice. *Am J Hum Genet* **105**:1168–1181. doi:10.1016/j.ajhg.2019.10.010

Liu C, Tu C, Wang L, Wu H, Houston BJ, Mastrorosa FK, Zhang W, Shen Y, Wang J, Tian S, Meng L, Cong J, Yang S, Jiang Y, Tang S, Zeng Y, Lv M, Lin G, Li J, Saiyin H, He X, Jin L, Touré A, Ray PF, Veltman JA, Shi Q, O'Bryan MK, Cao Y, Tan Y-Q, Zhang F. 2021. Deleterious variants in X-linked CFAP47 induce asthenoteratozoospermia and primary male infertility. *Am J Hum Genet* **108**:309–323. doi:10.1016/j.ajhg.2021.01.002

Liu W, He X, Yang S, Zouari R, Wang J, Wu H, Kherraf Z-E, Liu C, Coutton C, Zhao R, Tang D, Tang S, Lv M, Fang Y, Li W, Li H, Zhao J, Wang X, Zhao S, Zhang J, Arnoult C, Jin L, Zhang Z, Ray PF, Cao Y, Zhang F. 2019. Bi-allelic Mutations in TTC21A Induce Asthenoteratospermia in Humans and Mice. *Am J Hum Genet* **104**:738–748. doi:10.1016/j.ajhg.2019.02.020

Livak KJ, Schmittgen TD. 2001. Analysis of relative gene expression data using real-time quantitative PCR and the 2(-Delta Delta C(T)) Method. *Methods San Diego Calif* **25**:402–408. doi:10.1006/meth.2001.1262

Lorès P, Dacheux D, Kherraf Z-E, Nsota Mbango J-F, Coutton C, Stouvenel L, Ialy-Radio C, Amiri-Yekta A, Whitfield M, Schmitt A, Cazin C, Givelet M, Ferreux L, Fourati Ben Mustapha S, Halouani L, Marrakchi O, Daneshipour A, El Khouri E, Do Cruzeiro M, Favier M, Guillonneau F, Chaudhry M, Sakheli Z, Wolf J-P, Patrat C, Gacon G, Savinov SN, Hosseini SH, Robinson DR, Zouari R, Ziyyat A, Arnoult C, Dulioust E, Bonhivers M, Ray PF, Touré A. 2019. Mutations in TTC29, Encoding an Evolutionarily Conserved Axonemal Protein, Result in Asthenozoospermia and Male Infertility. *Am J Hum Genet* **105**:1148–1167. doi:10.1016/j.ajhg.2019.10.007

Lu Y, Oura S, Matsumura T, Oji A, Sakurai N, Fujihara Y, Shimada K, Miyata H, Tobita T, Noda T, Castaneda JM, Kiyozumi D, Zhang Q, Larasati T, Young SAM, Kodani M, Huddleston CA, Robertson MJ, Coarfa C, Isotani A, Aitken RJ, Okabe M, Matzuk MM, Garcia TX, Ikawa M. 2019. CRISPR/Cas9-mediated genome editing reveals 30 testis-enriched genes dispensable for male fertility in mice†. *Biol Reprod* **101**:501–511. doi:10.1093/biolre/ioz103

Luck K, Kim D-K, Lambourne L, Spirohn K, Begg BE, Bian W, Brignall R, Cafarelli T, Campos-Laborie FJ, Charloteaux B, Choi D, Coté AG, Daley M, Deimling S, Desbuleux A, Dricot A, Gebbia M, Hardy MF, Kishore N, Knapp JJ, Kovács IA, Lemmens I, Mee MW, Mellor JC, Pollis C, Pons C, Richardson AD, Schlabach S, Teeking B, Yadav A, Babor M, Balcha D, Basha O, Bowman-Colin C, Chin S-F, Choi SG, Colabella C, Coppin G, D'Amata C, De Ridder D, De Rouck S, Duran-Frigola M, Ennajdaoui H, Goebels F, Goehring L, Gopal A, Haddad G, Hatchi E, Helmy M, Jacob Y, Kassa Y, Landini S, Li R, van Lieshout N, MacWilliams A, Markey D, Paulson JN, Rangarajan S, Rasla J, Rayhan A, Rolland T, San-Miguel A, Shen Y, Sheykhkarimli D, Sheynkman GM, Simonovsky E, Taşan M, Tejeda A, Tropepe V, Twizere J-C, Wang Y, Weatheritt RJ, Weile J, Xia Y, Yang X, Yeger-Lotem E, Zhong Q, Aloy P, Bader GD, De Las Rivas J, Gaudet S, Hao T, Rak J, Tavernier J, Hill DE, Vidal M, Roth FP, Calderwood MA. 2020. A reference map of the human binary protein interactome. *Nature* **580**:402–408. doi:10.1038/s41586-020-2188-x

McLaren W, Gil L, Hunt SE, Riat HS, Ritchie GRS, Thormann A, Flicek P, Cunningham F. 2016. The Ensembl Variant Effect Predictor. *Genome Biol* **17**:122. doi:10.1186/s13059-016-0974-4

Meienberg J, Bruggmann R, Oexle K, Matyas G. 2016. Clinical sequencing: is WGS the better WES? *Hum Genet* **135**:359–362. doi:10.1007/s00439-015-1631-9

Nsota Mbango J-F, Coutton C, Arnoult C, Ray PF, Touré A. 2019. Genetic causes of male infertility: snapshot on morphological abnormalities of the sperm flagellum. *Basic Clin Androl* **29**:2. doi:10.1186/s12610-019-0083-9

O'Donnell L. 2014. Mechanisms of spermiogenesis and spermiation and how they are disturbed. *Spermatogenesis* **4**:e979623. doi:10.4161/21565562.2014.979623

Oud MS, Smits RM, Smith HE, Mastrorosa FK, Holt GS, Houston BJ, de Vries PF, Alobaidi BKS, Batty LE, Ismail H, Greenwood J, Sheth H, Mikulasova A, Astuti GDN, Gilissen C, McEleny K, Turner H, Coxhead J, Cockell S, Braat DDM, Fleischer K, D'Hauwers KWM, Schaafsma E, Genetics of Male Infertility Initiative (GEMINI) consortium, Nagirnaja L, Conrad DF, Friedrich C, Kliesch S, Aston KI, Riera-Escamilla A, Krausz C, Gonzaga-Jauregui C, Santibanez-Koref M, Elliott DJ, Vissers LELM, Tüttelmann F, O'Bryan MK, Ramos L, Xavier MJ, van der Heijden GW, Veltman JA. 2022. A de novo paradigm for male infertility. *Nat Commun* **13**:154. doi:10.1038/s41467-021-27132-8

Plagnol V, Curtis J, Epstein M, Mok KY, Stebbings E, Grigoriadou S, Wood NW, Hambleton S, Burns SO, Thrasher AJ, Kumararatne D, Doffinger R, Nejentsev S. 2012. A robust model for read count data in exome sequencing experiments and implications for copy number variant calling. *Bioinforma Oxf Engl* **28**:2747–2754. doi:10.1093/bioinformatics/bts526

Ralston KS, Kabututu ZP, Melehani JH, Oberholzer M, Hill KL. 2009. The Trypanosoma brucei flagellum: moving parasites in new directions. *Annu Rev Microbiol* **63**:335–62. doi:10.1146/annurev.micro.091208.073353

Ralston KS, Kisalu NK, Hill KL. 2011. Structure-function analysis of dynein light chain 1 identifies viable motility mutants in bloodstream-form Trypanosoma brucei. *Eukaryot Cell* **10**:884–94. doi:10.1128/EC.00298-10

Rolland M, Le Moal J, Wagner V, Royère D, De Mouzon J. 2013. Decline in semen concentration and morphology in a sample of 26,609 men close to general population between 1989 and 2005 in France. *Hum Reprod Oxf Engl* **28**:462–470. doi:10.1093/humrep/des415

Schindelin J, Arganda-Carreras I, Frise E, Kaynig V, Longair M, Pietzsch T, Preibisch S, Rueden C, Saalfeld S, Schmid B, Tinevez J-Y, White DJ, Hartenstein V, Eliceiri K, Tomancak P, Cardona A. 2012. Fiji - an Open Source platform for biological image analysis. *Nat Methods* **9**:10.1038/nmeth.2019. doi:10.1038/nmeth.2019

Schneider CA, Rasband WS, Eliceiri KW. 2012. NIH Image to ImageJ: 25 years of image analysis. *Nat Methods* **9**:671–675.

Schumann Burkard G, Jutzi P, Roditi I. 2011. Genome-wide RNAi screens in bloodstream form trypanosomes identify drug transporters. *Mol Biochem Parasitol* **175**:91–94. doi:10.1016/j.molbiopara.2010.09.002

Shamoto N, Narita K, Kubo T, Oda T, Takeda S. 2018. CFAP70 Is a Novel Axoneme-Binding Protein That Localizes at the Base of the Outer Dynein Arm and Regulates Ciliary Motility. *Cells* **7**. doi:10.3390/cells7090124

Sunter JD. 2016. A vanillic acid inducible expression system for Trypanosoma brucei. *Mol Biochem Parasitol* **207**:45–48. doi:10.1016/j.molbiopara.2016.04.001

Touré A, Martinez G, Kherraf Z-E, Cazin C, Beurois J, Arnoult C, Ray PF, Coutton C. 2020. The genetic architecture of morphological abnormalities of the sperm tail. *Hum Genet* **140**:21-42doi:10.1007/s00439-020-02113-x

Tyanova S, Temu T, Sinitcyn P, Carlson A, Hein MY, Geiger T, Mann M, Cox J. 2016. The Perseus computational platform for comprehensive analysis of (prote)omics data. *Nat Methods* **13**:731–740. doi:10.1038/nmeth.3901

Vincensini L, Blisnick T, Bastin P. 2011. 1001 model organisms to study cilia and flagella. *Biol Cell* **103**:109–130. doi:10.1042/BC20100104

Wang G, Guo Y, Zhou T, Shi X, Yu J, Yang Y, Wu Y, Wang J, Liu M, Chen X, Tu W, Zeng Y, Jiang M, Li S, Zhang P, Zhou Q, Zheng B, Yu C, Zhou Z, Guo X, Sha J. 2013. In-depth proteomic analysis of the human sperm reveals complex protein compositions. *J Proteomics* **79**:114–122. doi:10.1016/j.jprot.2012.12.008

Wang W-L, Tu C-F, Tan Y-Q. 2020. Insight on multiple morphological abnormalities of sperm flagella in male infertility: what is new? *Asian J Androl* **22**:236–245. doi:10.4103/aja.aja_53_19

Wang Y, Yang J, Jia Y, Xiong C, Meng T, Guan H, Xia W, Ding M, Yuchi M. 2014. Variability in the morphologic assessment of human sperm: use of the strict criteria recommended by the World Health Organization in 2010. *Fertil Steril* **101**:945-9. doi:10.1016/j.fertnstert.2013.12.047

Wickstead B, Gull K. 2007. Dyneins Across Eukaryotes: A Comparative Genomic Analysis. *Traffic* **8**:1708–1721. doi:10.1111/j.1600-0854.2007.00646.x

Wirtz E, Leal S, Ochatt C, Cross GeorgeAM. 1999. A tightly regulated inducible expression system for conditional gene knock-outs and dominant-negative genetics in Trypanosoma brucei. *Mol Biochem Parasitol* **99**:89–101. doi:10.1016/S0166-6851(99)00002-X

Woods A, Sherwin T, Sasse R, MacRae TH, Baines AJ, Gull K. 1989. Definition of individual components within the cytoskeleton of Trypanosoma brucei by a library of monoclonal antibodies. *J Cell Sci* **93 (Pt 3)**:491–500.

Yamamoto R, Hwang J, Ishikawa T, Kon T, Sale WS. 2021. Composition and function of ciliary inner-dynein-arm subunits studied in Chlamydomonas reinhardtii. *Cytoskelet Hoboken NJ* **78**:77–96. doi:10.1002/cm.21662

Yamamoto R, Yagi T, Kamiya R. 2006. Functional binding of inner-arm dyneins with demembranated flagella of Chlamydomonas mutants. *Cell Motil Cytoskeleton* **63**:258–265. doi:10.1002/cm.20121

Yamamoto R, Yanagisawa H, Yagi T, Kamiya R. 2008. Novel 44-Kilodalton Subunit of Axonemal Dynein Conserved from Chlamydomonas to Mammals. *Eukaryot Cell* **7**:154–161. doi:10.1128/EC.00341-07

Acknowledgments: We thank all individuals for their participation. We thank Samuel Dean (Warwick Medical School) and Jack Sunter (Oxford Brookes University) for the pPOT plasmids and SmOx T. brucei cell lines, F. Bringaud (University of Bordeaux) for the anti-enolase antibody, P. Bastin (Institut Pasteur) for the anti-Ty1 antibody. We thank G. Cougnet-Houlery, S. Guit, and J. Marcos for ongoing access to the MFP lab infrastructure. This work was supported by the Institut National de la Santé et de la Recherche Médicale (INSERM), the Centre National de la Recherche Scientifique (CNRS), University Grenoble Alpes, and French National Research Agency funding for specific projects: MASFLAGELLA (ANR-14-CE15-0002), FLAGEL-OME (ANR-19-CE17-0014), OLIGO-SPERM (ANR-21-CE17-0007). Mass spectrometry experiments were performed at the Centre de Génomique Fonctionnelle facility (CGFB, Bordeaux) for Trypanosoma studies and at the Proteom'IC core-facility (Institut Cochin, Paris - François Guillonneau and Johanna Bruce) for mouse studies. The Orbitrap Fusion mass spectrometer at the Proteom'IC core-facility was acquired with funds from the FEDER through the « Operational Program for Competitiveness Factors and employment 2007-2013 » and from the « Cancéropôle Ile-de-France ». The Bordeaux Imaging Center is a service unit of the CNRS INSERM and Bordeaux University, a member of the French BioImaging national infrastructure funded through the French National Research Agency [ANR-10-INBS-04]. **Author contributions:** D.D., M.Bo., G.M., P.F.R., Z-E.K., C.Ca., C.L., E.L., M.Bi., C.A., A.T. and C.Co. analyzed the data and wrote the manuscript; C.Co., Z.-E.K., C.Ca., G.M., M.Bi., A.S., and N.T.-M. performed and analyzed the genetic data; D.D., C.E.B.R., D.R.R., M.T., J-W.D., and M.Bo. performed the Trypanosoma studies. J.B. and G.M. performed the immunofluorescence assays. P.L. and A.T. performed studies on the *Ttc29*$^{-/-}$ mouse model. A.A.-Y., A.D., S.-H.H., X.J., Y.S., C.L., R.H., L.H., and V.S. provided clinical samples and data; G.M., P.F.R., A.T., D.D., M.Bo., and C.Co. designed the study, supervised all molecular laboratory work, had full access to all study data, and took responsibility for data integrity and accuracy. All authors have read and agreed to the published version of the manuscript. **Competing interests:** The authors declare no competing interests. **Data and materials availability:** All data needed to evaluate the conclusions presented in the paper are provided in the paper and/or the Supplementary Materials.

Supplementary Materials for

Novel axonemal protein ZMYND12 interacts with TTC29 and DNAH1, and is required for male fertility and flagellum function.

Denis Dacheux *et al.*

*Corresponding author. Email: CCoutton@chu-grenoble.fr

This PDF file includes:

Supplementary Text

Figs. S1 to S10

Tables S1 to S7

Movies S1 to S2

References

Supplementary text

Whole-Exome Sequencing (WES) and bioinformatics analysis

Genomic DNA was isolated from EDTA blood using DNeasy Blood & Tissue Kits (QIAGEN SA). Genetic data were obtained through several sequencing centers, in particular Novogene, Genoscope, and Integragen. Coding regions and intron/exon boundaries were sequenced after enrichment using Agilent SureSelect Human All Exon V5, V6, or Clinical Research capture kits.

An alignment-ready GRCh38 reference genome (including ALT, decoy, and HLA) was produced using "run-gen-ref hs38DH" from Heng Li's bwakit package (https://github.com/lh3/bwa). Exomes were analyzed using a bioinformatics pipeline developed in-house. The pipeline consists of two modules, both distributed under the GNU General Public License v3.0 and available on github (grexome-TIMC-Primary and grexome-TIMC-Secondary, URLs indicated in the web resources).

The first module takes FASTQ files as input and produces a single merged GVCF file per variant-caller, as follows: trim adaptors and filter low-quality reads with fastp 0.23.2, align reads with BWA-MEM 0.7.17, mark duplicates using samblaster 0.1.26, and sort and index BAM files with samtools 1.15.1. SNVs and short indels are called from each BAM file using strelka 2.9.10 (Kim et al., 2018) and GATK 4.1.8.1 to produce individual GVCF files from each variant-caller. These files are finally merged using mergeGVCFs.pl to obtain a single multi-sample GVCF per caller. Using several variant-callers helps to compensate for each caller's flaws.

The second module takes each merged GVCF as input and produces annotated analysis-ready TSV files. Annotation involved 17 streamlined tasks: Low-quality variant calls (DP < 10, GQ < 20, or less than 15% of reads supporting the ALT allele) were discarded. Variant Effect

Predictor v108 (McLaren et al., 2016) was used to annotate variants and predict their impact, in order to filter out low-impact (MODIFIER) variants and/or prioritize high-impact ones (e.g., stop-gain or frameshift variants). Variants with a minor allele frequency greater than 1% in gnomAD v.2.1 or 3% in 1000 Genomes Project phase 3 were excluded. The pipeline performs an integrative analysis of all available exomes, both at the individual variant level and at the gene level. Thus, recurring genomic variants are readily identified alongside genes that are severely impacted in several patients but not in control subjects. Additional information can be found in Arafah et al. (Arafah et al., 2021). Copy number variants (CNVs) were searched using the ExomeDepth software package, as previously reported (Kherraf et al., 2018; Plagnol et al., 2012).

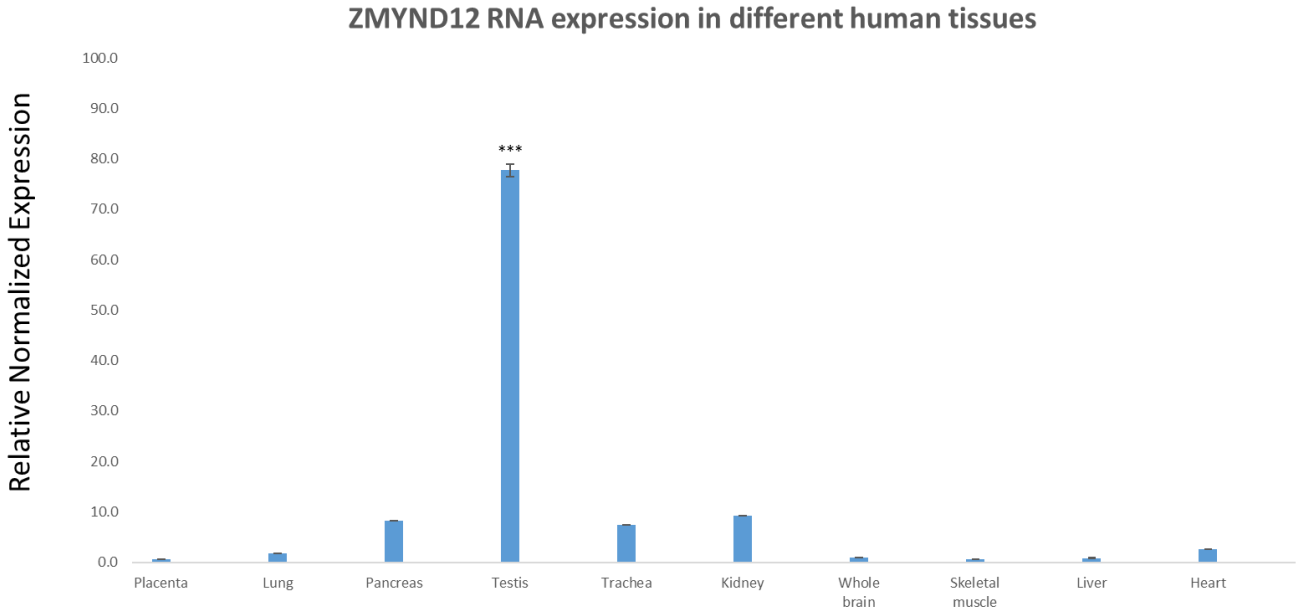

Fig. S1. Relative mRNA Expression of human *ZMYND12* transcripts. RT-qPCR was performed with cDNAs from various human tissues purchased from Life Technologies®. A panel of 10 organs was used for experiments: placenta, lung, pancreas, testis, trachea, kidney, whole brain, skeletal muscle, liver and heart. Each sample was assayed in triplicate for each gene on a StepOnePlus (Life Technologies®) with Power SYBR®Green PCR Master Mix (Life Technologies®). The PCR cycle was as follows: 10 min at 95 °C, 1 cycle for enzyme activation; 15 s at 95 °C, 60 s at 60 °C with fluorescence acquisition, 40 cycles for the PCR. RT-qPCR data were normalized using the two reference housekeeping genes *RPL6* and *RPL27* for human samples, applying the $-\Delta\Delta C_t$ method(Livak and Schmittgen, 2001). The $2^{-\Delta\Delta Ct}$ value was set to 0 in brain cells, resulting in an arbitrary maximum expression of 1. The efficacy of primers was checked using a standard curve. Melting curve analysis was used to verify the presence of a single PCR product. Statistical significance of differences in expression of *ZMYND12* transcripts in several organs was determined by applying a two-tailed *t*-test using Prism 4.0 software (GraphPad, San Diego, CA). ***P< 0.001.

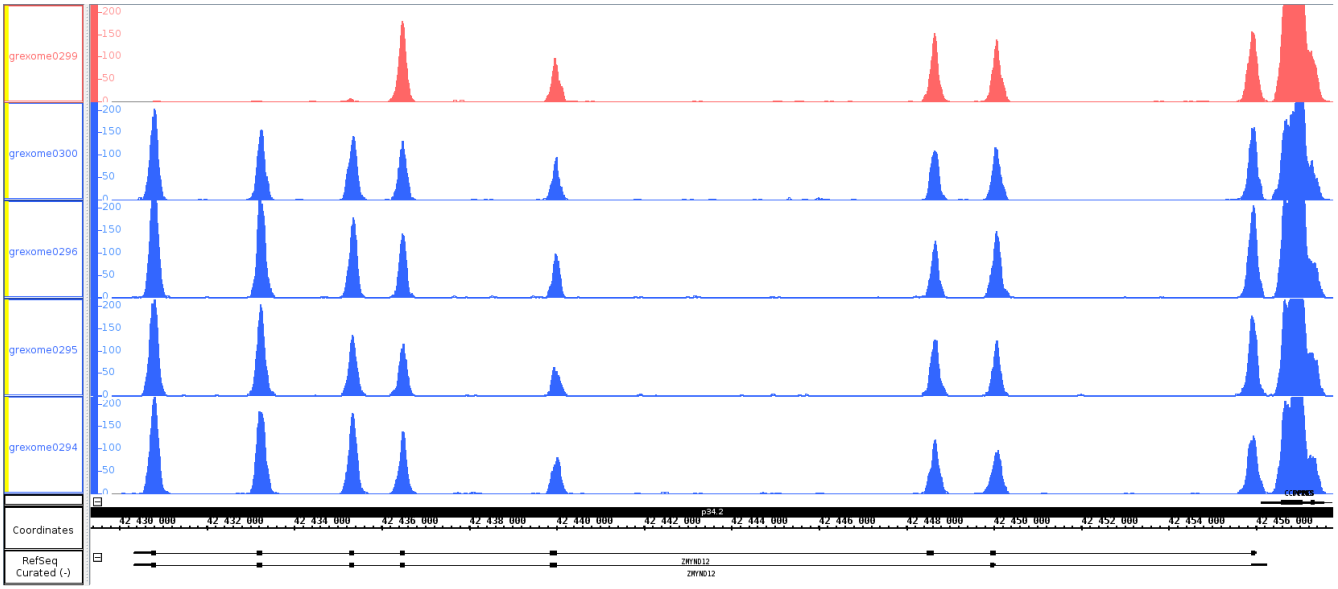

Fig. S2. Depth of coverage at the *ZMYND12* locus for the ZMYND12_2 individual, carrier of a homozygous deletion of exons 6-8, and four other unrelated MMAF individuals. Compared with the control individuals (blue), affected individual ZMYND12_2 (red) showed a complete absence of sequence coverage for exons 6, 7 and 8. ZMYND12 is on the reverse genomic strand. The five samples shown were processed by exome-seq in a single batch, using the same Agilent Clinical Research capture kit, Illumina HiSeq 4000 sequencing technology, and bioinformatics pipeline (see Supplemental Methods).

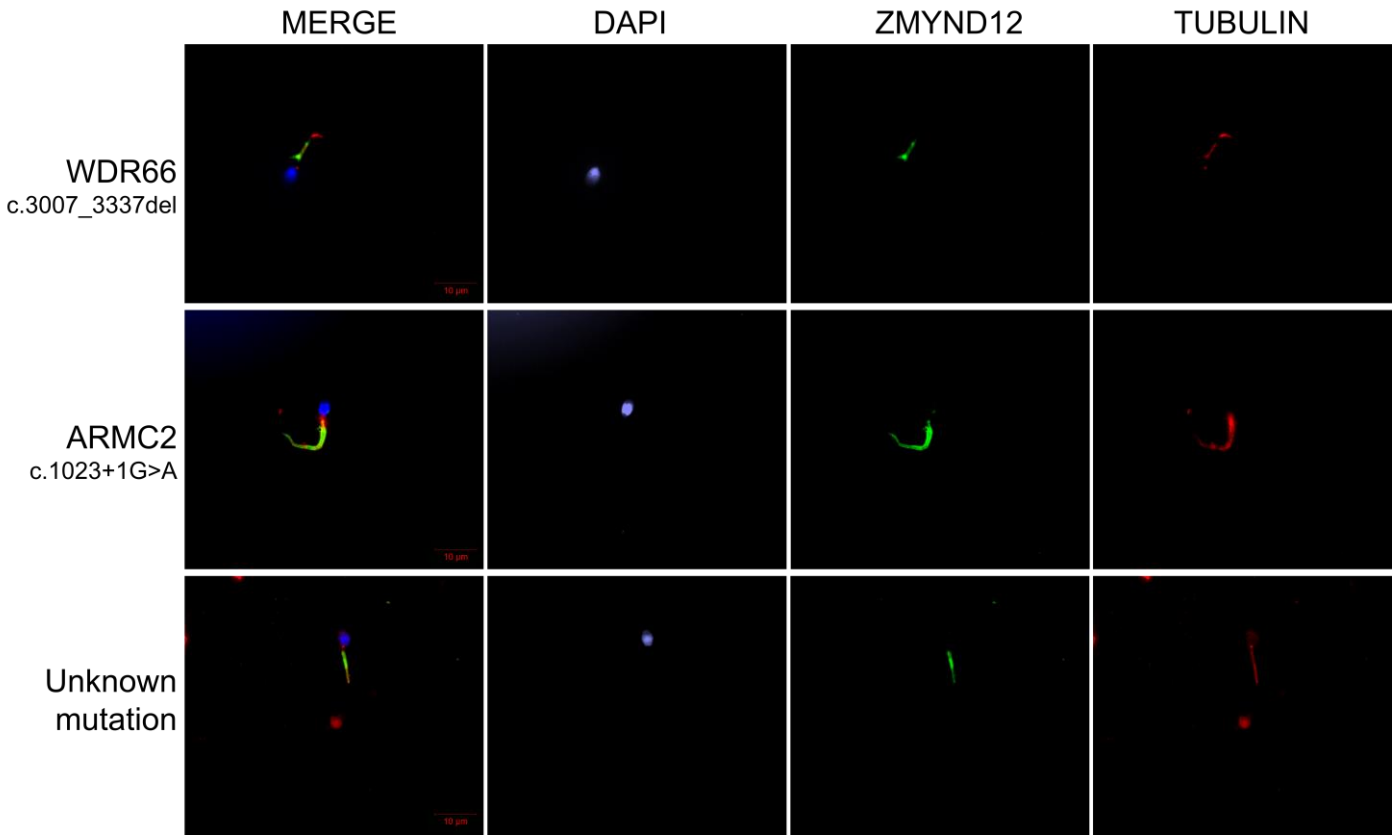

Fig. S3. ZMYND12 immunostaining in human spermatozoa from MMAF individuals carriers of pathogenic variants in *ARMC2* and *WDR66* genes, or with unknwon genetic cause. Sperm cells from a fertile control individual, two MMAF patients, carriers of mutations in *ARMC2* and *WDR66*, and one MMAF patient with unknown genetic cause were stained with anti-ZMYND12 (green) and anti-acetylated tubulin (red) antibodies. Sperm nuclear DNA was counterstained with DAPI (blue). ZMYND12 immunostaining was present throughout the flagellum in all samples, regardless of phenotype. Variants are specified for each patient. Scale bars: 10 μm.

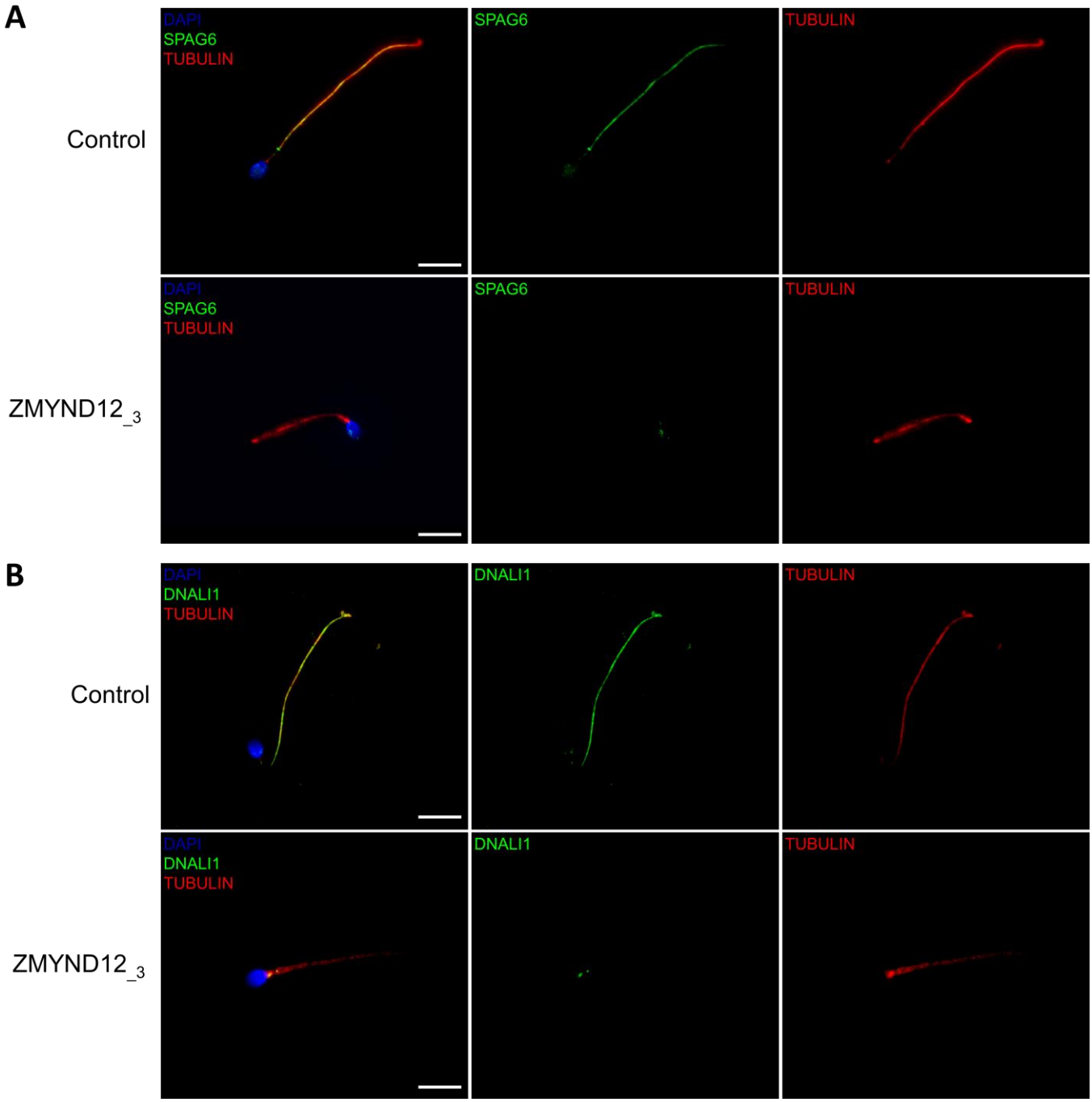

Fig. S4. Altered immunostaining for SPAG6 and DNALI1 in the presence of *ZMYND12* variants. Immunofluorescence experiments were performed using sperm cells from control individuals and from individual ZMYND12_3 carrying the nonsense variant c.433C>T. Although tubulin staining remained detectable, sperm cells from individual ZMYND12_3 showed no immunostaining for (A) SPAG6 and (B) DNALI1. The CPC and the IDAs were therefore strongly disorganized in these cells. Scale bars: 10 µm.

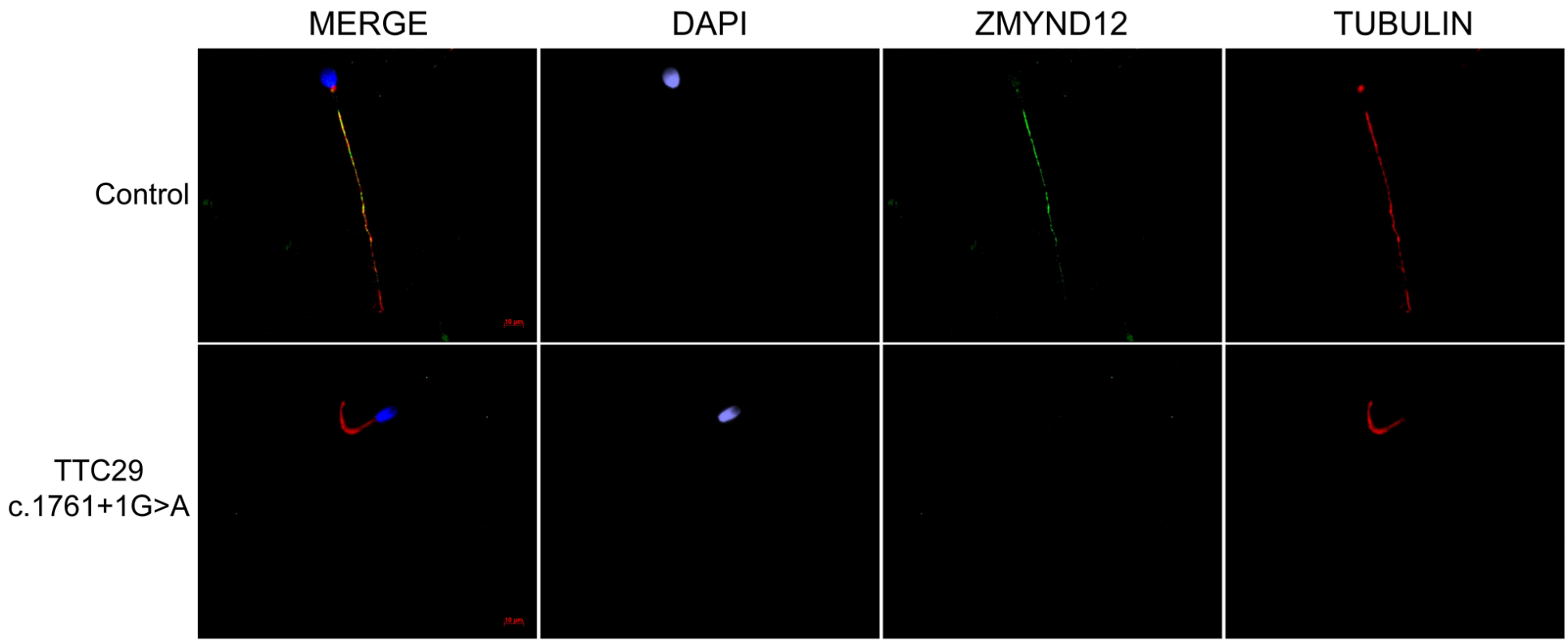

Fig. S5. ZMYND12 is absent from sperm cells from *TTC29* individuals. Sperm cells from a fertile control individual and a TTC29 individual carrying the previously-reported c.1761+1G>A splice-variant (Lorès et al., 2019) were stained with anti-ZMYND12 (green) and anti-acetylated tubulin (red) antibodies. DAPI counterstaining was used to reveal sperm nuclear DNA (blue). In control sperm, ZMYND12 immunostaining decorated the full length of the flagellum, but in sperm from TTC29 individuals, a total absence of ZMYND12 was recorded. Scale bars: 10 μm.

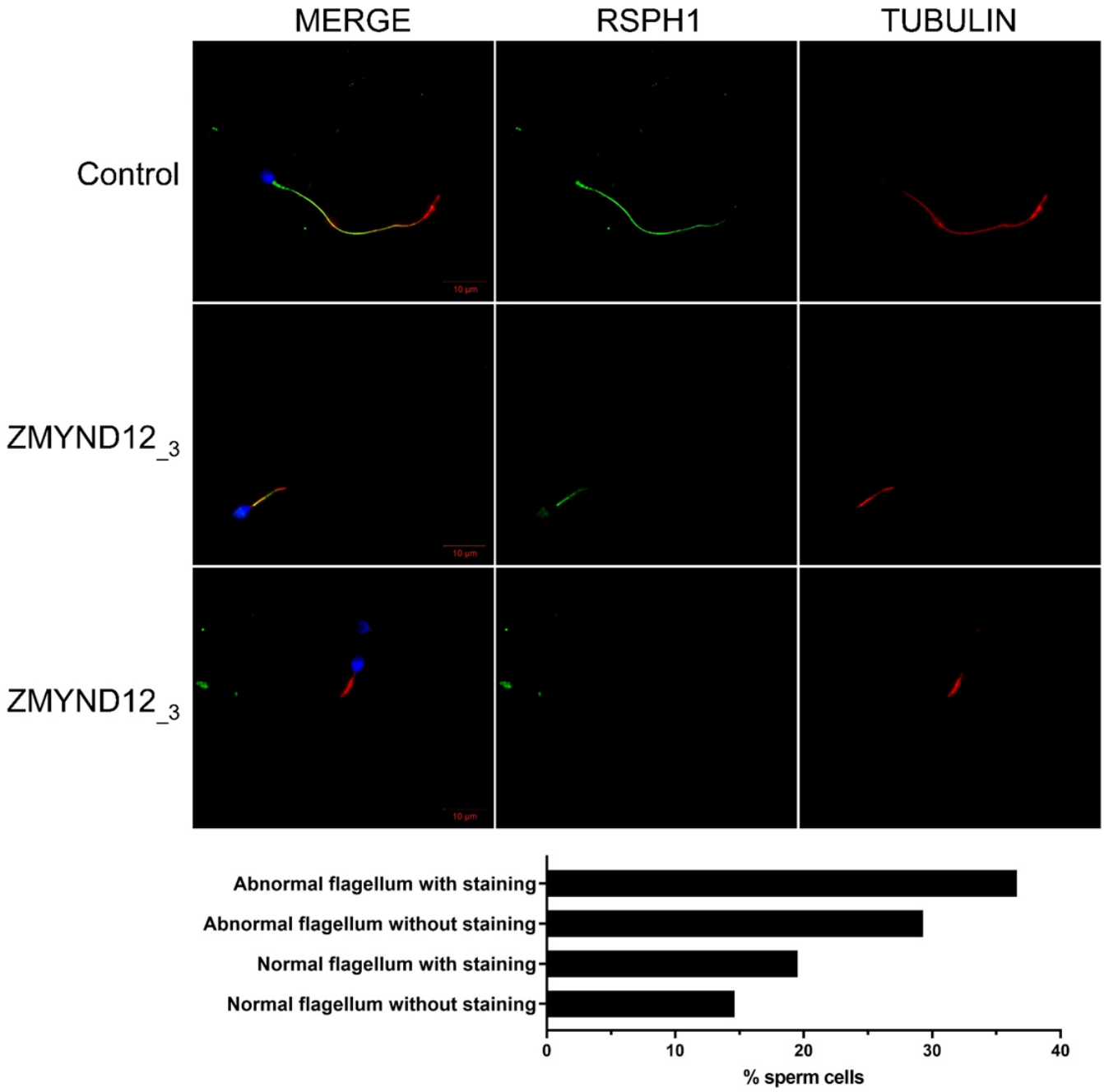

Fig. S6. Radial spokes are inconstantly affected in *ZMYND12* individuals. Sperm cells from a fertile control individual and from individual ZMYND12_3 stained with anti-RSPH1 (green) – located in the radial spokes – and anti-acetylated tubulin (red) antibodies. RSPH1 immunostaining is uniformly present along the length of the flagellum in control sperm cells. Sperm cells from individual ZMYND12_3 show heterogeneous staining regardless of flagellar morphology, suggesting that the radial spokes are inconsistently present in sperm cells from

this individual. Scale bars: 10 µm. Lower panel: Histogram showing the percentage of analyzed spermatozoa of various morphologies displaying or lacking RSPH1 immunostaining (number of sperm cells analyzed = 200).

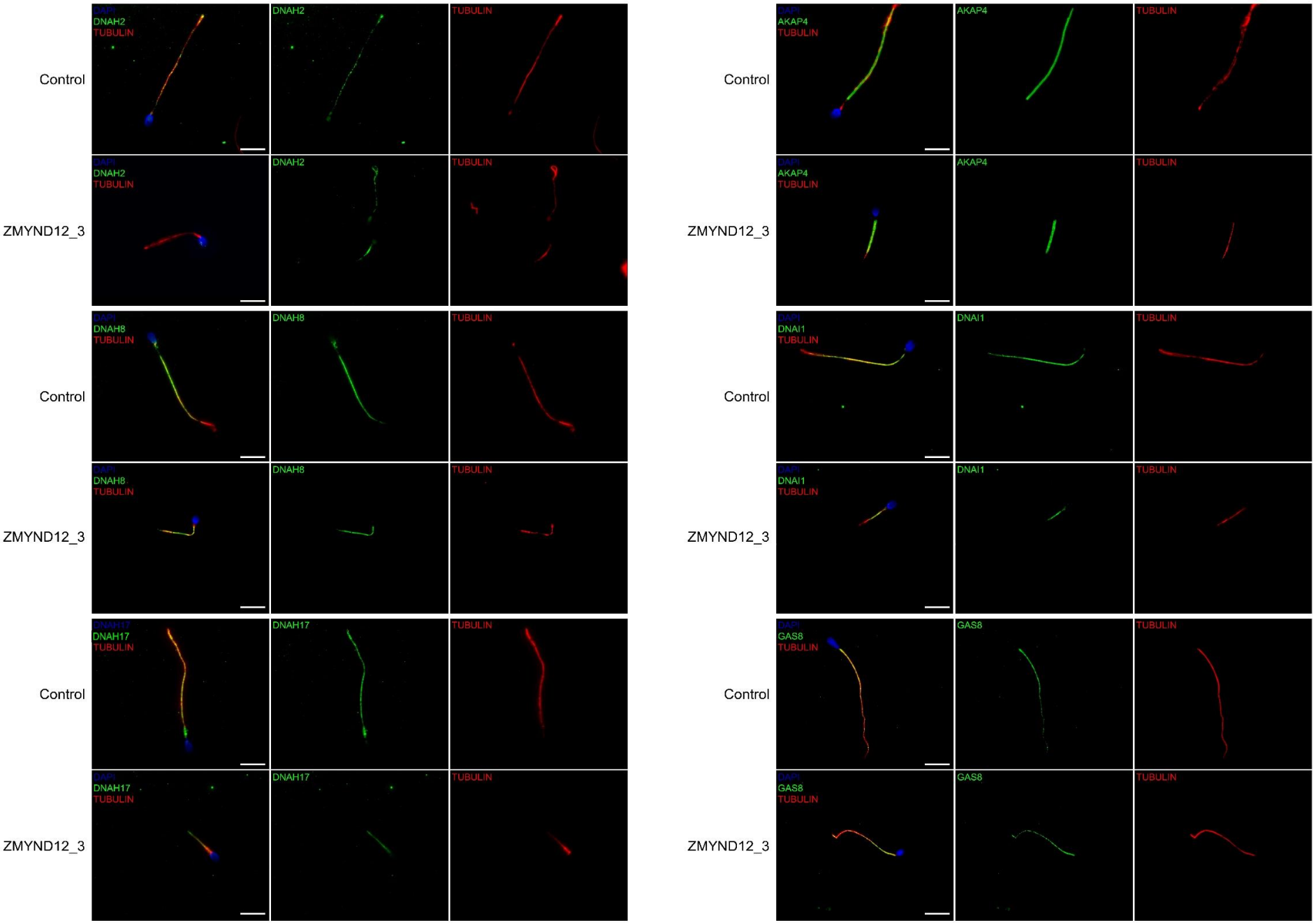
Control
ZMYND12_3
DAPI
DNAH2
TUBULIN
DNAH2
TUBULIN
AKAP4
GAS8
DNAI1
DNAH8
DNAH17

Fig. S7. Immunostaining for AKAP4, DNAH2, DNAH8, DNAH17, DNAI1, and GAS8 is not affected by *ZMYND12* mutation. Immunofluorescence (IF) experiments were performed using sperm cells from control individuals and from individual ZMYND12_3, carrier of the nonsense variant c.433C>T. Immunostaining patterns for AKAP4, DNAH2, DNAH8, DNAH17, DNAI1, and GAS8 in sperm from individual ZMYND12_3 were comparable to those observed in control sperm cells, demonstrating that the fibrous sheath, outer dynein arms (ODAs) and the N-DRC were not directly affected by *ZMYND12* variants. Scale bars: 10 µm.

A

```
ZYMND12 MNVIYPLAVPKGRRLCCEVCEAPAERVCAACTVTYYCGVVHQKADWDSIHEKICQLLIPL
TbTAX-1 ---------MQGANL----KVLPSTRAAAK---ELVDPLDITNVGWSTLEPKFDELMQLM
                  :* .* *: *..* : :..*.::. *: :*: :

ZYMND12 RTSMPFYNSEEERQHGLQQLQQRQKYLIEFCYTIAQKYLFEGKHEDAVPAALQSLRFRVK
TbTAX-1 DAPSSGINALAARSAHREKVGAVIEQLLTRAQDESRRLLVEGNGEAAAEAGVKTLRLKER
         : *: *. ::: : *: . ::: *.**: * *. *.:::**:: :

ZYMND12 LYGLSSVELVPAYLLLAEASLGLGRIVQAEEYLFQAQWTVLKSTDCSN-ATHSLLHRNLG
TbTAX-1 FYGKGSVKLVPAHFHLARTNQFLKRYGNAEEILSLAHFIILQNPDEADATIKAELHQTFG
         :** .**:****:: **.:. * * :*** * *:: :*:. * :: : :: **:.:*

ZYMND12 LLYIAKKNYEEARYHLANDIYFASCAFGTEDIRTSGGYFHLANIFYDLKKLDLADTLYTK
TbTAX-1 LLYAADNKLDVSVKHLTCATYYLSVMNGPEHVLTTFAYFDLANVFATKACMEAAMALYDT
         *** *.:: : : **: *: * * *.: *: .**.***:* :: * :** .

ZYMND12 VSEIWHAYLNNHYQVLSQAHIQQMDLLGKLFENDTGLDEA----------QEAEAIRIL
TbTAX-1 VKNIWLKHLRRVLKDIVDETMAA--KLVKRYDDDEVTHEVGHASARAFGKENLADVSKML
         *.:** :*.. : : : : * * :::* .*. : *:. ::*

ZYMND12 TSILNIRES---TSDKAPQKTIFVLKILVMFYYLMMNSSKAQEYGMRALSLAKEQQLDVH
TbTAX-1 FGIFSIQKERLTISHPTTARAQFLLG----LYLLWVNKNDEAA--EHLLSAR--------
          .*:.*::. *. : :: *:* :* * :*... : **

ZYMND12 EQSTIQELLSLISTEDHPIT----------------------
TbTAX-1 --TT----SQKFYGERHPIVQDIEDWCIWFEIPFRGVAAEQ
          :* . : * ***.
```

B

Fig. S8. TbTAX-1 is the *T. brucei* ortholog of ZMYND12. (**A**) Clustal Omega alignment of human ZYMND12 and TbTAX-1. (**B**) Schematic representation of wild-type and truncated forms of ZYMND12 and TbTAX-1.

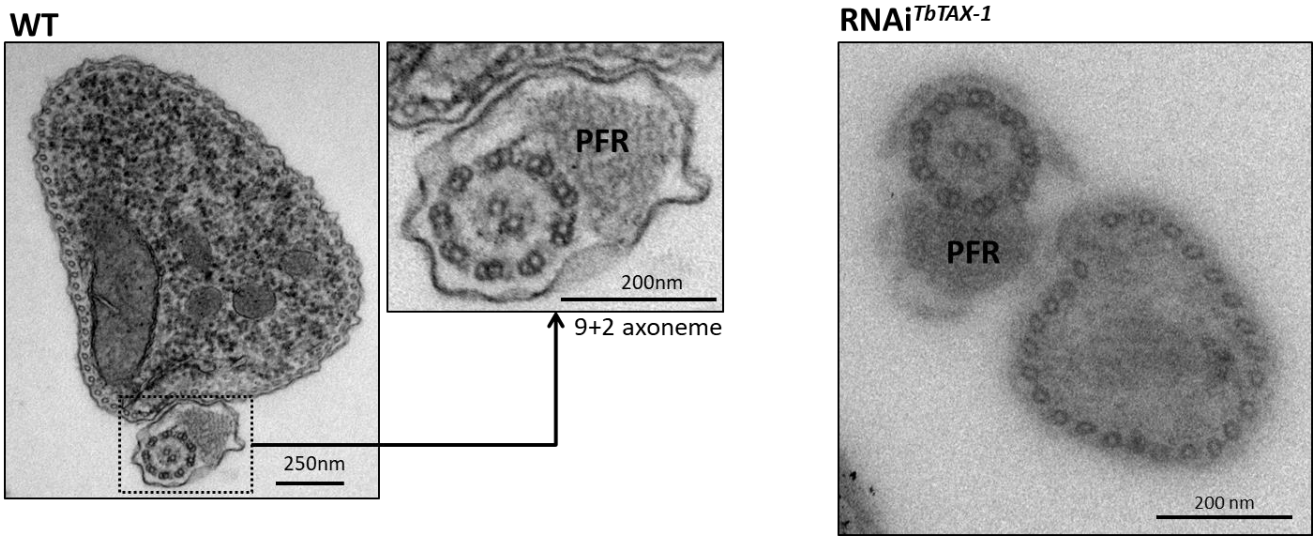

Fig. S9. TbTAX-1 RNAi knock-down. Micrograph of WT cells and TbTAX-1 RNAi-induced cells (48 h) in thin section. The characteristic 9+2 structure of the axoneme and the paraflagellar structure (PFR) are visible, and no obvious structural defects are observed in RNAi-induced cells.

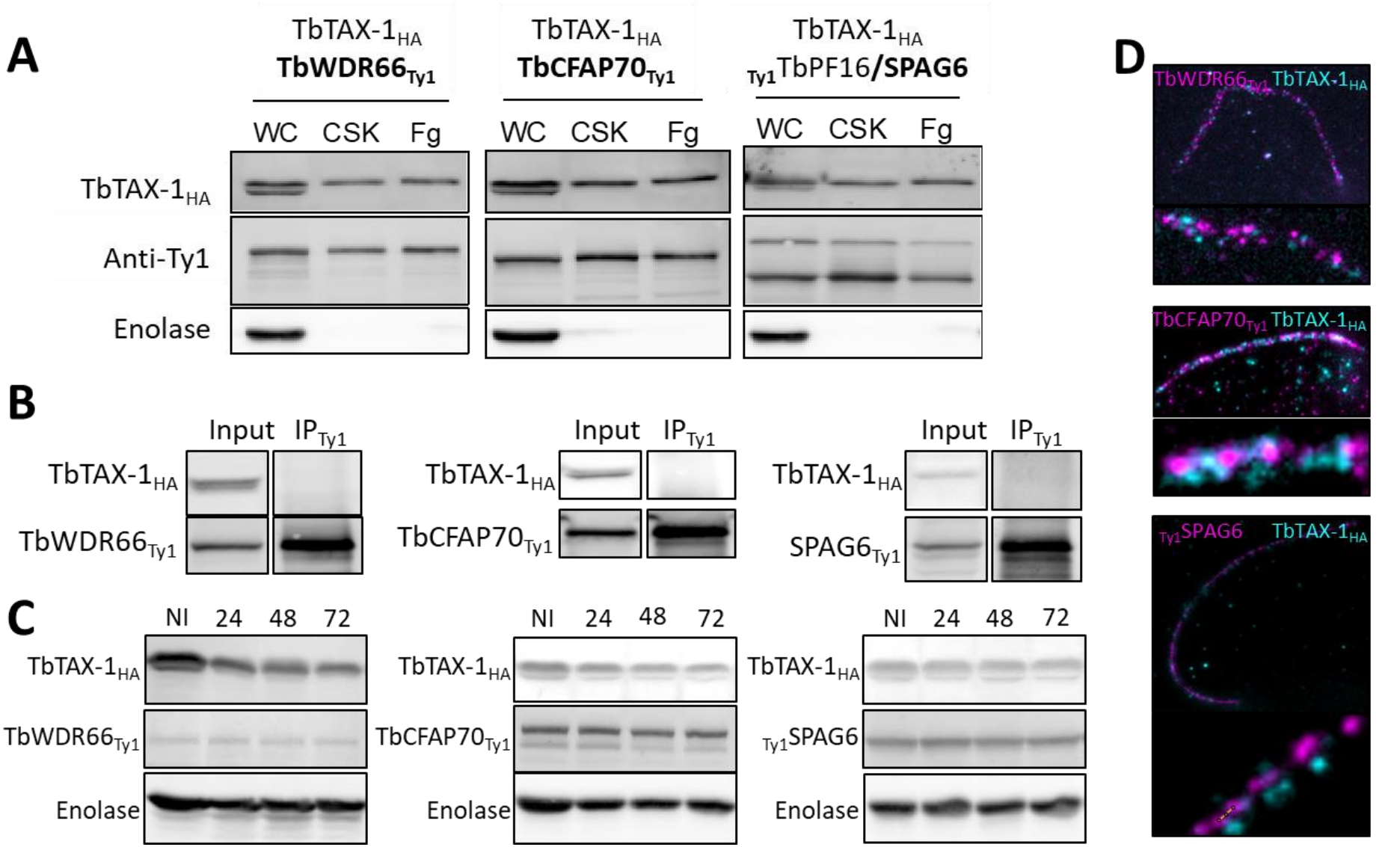
A
TbTAX-1HA
TbWDR66Ty1
TbTAX-1HA
TbCFAP70Ty1
TbTAX-1HA
Ty1TbPF16/SPAG6
WC CSK Fg
WC CSK Fg
WC CSK Fg
TbTAX-1HA
Anti-Ty1
Enolase
B
Input IPTy1
Input IPTy1
Input IPTy1
TbTAX-1HA
TbWDR66Ty1
TbTAX-1HA
TbCFAP70Ty1
TbTAX-1HA
SPAG6Ty1
C
NI 24 48 72
NI 24 48 72
NI 24 48 72
TbTAX-1HA
TbWDR66Ty1
Enolase
TbTAX-1HA
TbCFAP70Ty1
Enolase
TbTAX-1HA
Ty1SPAG6
Enolase
D
TbWDR66Ty1 TbTAX-1HA
TbCFAP70Ty1 TbTAX-1HA
Ty1SPAG6 TbTAX-1HA

Fig. S10. TbTAX-1 knock-down does not affect TbWDR66, TbCFAP70, or TbSPAG6. (**A**) TbWDR66, TbCFAP70, and TbSPAG6 are axoneme-associated proteins according to western blot analysis of whole cell lysate (WC), detergent-extracted cytoskeletons (CSK), salt-extracted flagella (Fg). Enolase was used as extraction control for cytoskeleton and flagella samples. (**B**) Co-immunoprecipitation assays using anti-Ty1 (IP_{Ty1}) in cell lines expressing TbTAX-1_{HA} alongside TbWDR66$_{Ty1}$ or TbCFAP70 or TbSPAG6$_{Ty1}$. Proteins were detected simultaneously by western blotting using anti-Ty1 and anti-HA antibodies and their corresponding fluorescent secondary antibodies.

(**C**) Western blot analysis of the fate of TbWDR66$_{Ty1}$, TbCFAP70$_{Ty1}$, or TbPF16/SPAG6$_{Ty1}$ in TbTAX-1 RNAi cells; non-induced (NI) cells, and cells induced for 24, 48, or 72 h. Enolase served as loading control. (**D**) U-ExM co-immunolabelling of TbTAX-1_{HA} (cyan) and TbWDR66$_{Ty1}$, TbCFAP70$_{Ty1}$, or TbSPAG6$_{Ty1}$ (magenta).

Table S1. Proteins co-immunoprecipitated with TbTAX-1 and TbTTC29 identified by mass spectrometry analyses.

TbTAX-1$_{HA}$ immunoprecipitation		
Accession number	**Protein**	**Fold-enrichment**
Tb927.9.10370	TbTAX-1 (Broadhead et al., 2006)	20.6
Tb927.3.1990	TbTTC29 (Lorès et al., 2019)	20.3
Tb927.11.8160	Dynein Heavy Chain putative. DNAH1 ortholog putative (Dean et al., 2016)	6.66
Tb927.10.15350	Histone H3 variant V	6.25
Tb927.10.14680	Ribosome biogenesis, putative	5.88
Tb927.11.3880	TrypARP, Actin putative(Ersfeld and Gull, 2001)	5.7
Tb927.11.3830	Hypothetical protein, conserved	4.42
Tb927.10.8940	Flagellum targeting protein kharon1	4.24
Tb927.11.970	Hypothetical protein, conserved	4.1
Tb927.10.170	Pseudouridine synthase, Cbf5p	3.7
Tb927.9.12610	Glycerol kinase, glycosomal	3.7
Tb927.2.2950	Nop14-like family, putative	3.5
Tb11.v5.0732.1	Hexokinase, putative	3.1
Tb927.11.16720	Mitotic cyclin 6, CYC6	2.4
Tb927.11.8870	DEAD-box ATP-dependent RNA helicase, MHEL61	2.3

TbTTC29$_{TY1}$ immunoprecipitation		
Accession number	**Protein**	**Fold-enrichment**
Tb927.3.1990	TbTTC29 (Lorès et al., 2019)	27.3
Tb927.11.8160	Dynein Heavy Chain putative. DNAH1 ortholog putative (Dean et al., 2016)	9.2
Tb927.9.10370	TbTAX-1 (Broadhead et al., 2006)	8.6
Tb927.11.11330	HSP70	6. 5
Tb927.11.3880	TrypARP, Actin putative(Ersfeld and Gull, 2001)	5.88
Tb927.3.1790	Pyruvate dehydrogenase E1 beta subunit, putative	2.4

Table S2. Proteins identification by tandem mass spectrometry (MS/MS) analysis of proteins co-immunoprecipitated with TTC29 from wild-type and Ttc29$^{-/-}$ L5 and L7 mouse testes.

Analysis of the 124 proteins specifically identified in wild-type testis

In blue, proteins identified in all 4 experimental replicates : n=3

In yellow, proteins identified in 3 out of 4 experimental replicates : n= 4

In grey, proteins identified in 2 out of 4 experimental replicates : n= 24

In white , proteins identified in 1 out of 4 experimental replicates : n= 93

Selected proteins	Peptides number per genotype and distribution per replicate									MW (kDa)	Protein Description	Species
	WT			L5 KO			L7 KO					
DYH1_MOUSE	153	4	55-47-30-21	-			-			487.1	Dynein heavy chain 1, axonemal	Mus musculus OX=10090
IDLC_MOUSE	33	4	5-13-9-6	-			-			29.7	Axonemal dynein light intermediate polypeptide 1	Mus musculus OX=10090
TTC29_MOUSE	31	4	4-10-10-7	-			-			54.3	Tetratricopeptide repeat protein 29	Mus musculus OX=10090
PRS8_MOUSE	8	3	4-2-2-0	-			-			35.7	Aldo-keto reductase family 1 member B1	Mus musculus OX=10090
BASI_MOUSE	5	3	3-1-1-0	-			-			59.8	ATP synthase subunit alpha, mitochondrial	Mus musculus OX=10090
MPCP_MOUSE	3	3	1-1-1-0	-			-			45.6	26S proteasome regulatory subunit 8	Mus musculus OX=10090
RL14_MOUSE	3	3	1-1-1-0	-			-			44.9	Phosphoglycerate kinase 2	Mus musculus OX=10090
ALDR_MOUSE	8	2	6-2-0-0	-			-			50.2	RuvB-like 1	Mus musculus OX=10090
ATPA_MOUSE	8	2	6-0-2-0	-			-			114.9	Sarcoplasmic/endoplasmic reticulum calcium ATPase 2	Mus musculus OX=10090
RUVB1_MOUSE	7	2	6-1-0-0	-			-			26.7	40S ribosomal protein S3	Mus musculus OX=10090
RUVB2_MOUSE	6	2	4-2-0-0	-			-			51.1	RuvB-like 2	Mus musculus OX=10090
ABCF2_MOUSE	4	2	1-3-0-0	-			-			58.0	T-complex protein 1 subunit zeta	Mus musculus OX=10090
ADT1_MOUSE	4	2	3-1-0-0	-			-			42.4	Basigin	Mus musculus OX=10090
ARL3_MOUSE	4	2	2-0-2-0	-			-			136.3	Cullin-associated NEDD8-dissociated protein 1	Mus musculus OX=10090
DHB4_MOUSE	4	2	3-0-1-0	-			-			111.2	Hypoxia up-regulated protein 1	Mus musculus OX=10090
RAB6A_MOUSE	4	2	3-0-1-0	-			-			57.1	Protein disulfide-isomerase	Mus musculus OX=10090
RB11A_MOUSE	4	2	0-2-2-0	-			-			68.5	Dolichyl-diphosphooligosaccharide--protein glycosyltransferase subunit 1	Mus musculus OX=10090
SRSF2_MOUSE	4	2	2-0-2-0	-			-			95.9	Protein 4.1	Mus musculus OX=10090
CKAP4_MOUSE	3	2	2-0-1-0	-			-			71.8	ATP-binding cassette sub-family F member 2	Mus musculus OX=10090
HVM03_MOUSE	3	2	0-1-2-0	-			-			32.9	ADP/ATP translocase 1	Mus musculus OX=10090
RS14_MOUSE	3	2	1-2-0-0	-			-			20.5	ADP-ribosylation factor-like protein 3	Mus musculus OX=10090
RSPH1_MOUSE	3	2	0-2-1-0	-			-			16.8	Calmodulin-1	Mus musculus OX=10090
ACYP1_MOUSE	2	2	1-1-0-0	-			-			79.5	Peroxisomal multifunctional enzyme type 2	Mus musculus OX=10090
DOPD_MOUSE	2	2	1-1-0-0	-			-			123.6	Importin-5	Mus musculus OX=10090
HMGA1_MOUSE	2	2	1-0-1-0	-			-			72.0	Protein disulfide-isomerase A4	Mus musculus OX=10090
HNRPL_MOUSE	2	2	0-1-1-0	-			-			24.9	Peroxiredoxin-6	Mus musculus OX=10090
KAP2_MOUSE	2	2	1-1-0-0	-			-			47.4	26S proteasome non-ATPase regulatory subunit 11	Mus musculus OX=10090
PPT1_MOUSE	2	2	1-0-1-0	-			-			23.6	Ras-related protein Rab-6A	Mus musculus OX=10090
SMIM4_MOUSE	2	2	1-0-0-1	-			-			24.4	Ras-related protein Rab-11A	Mus musculus OX=10090
STX12_MOUSE	2	2	0-1-1-0	-			-			25.5	Serine/arginine-rich splicing factor 2	Mus musculus OX=10090
U5S1_MOUSE	2	2	2-1*-0-0	-			-			139.9	Tripeptidyl-peptidase 2	Mus musculus OX=10090
PGK2_MOUSE	7	1	7-0-0-0	-			-			69.6	Xaa-Pro aminopeptidase 1	Mus musculus OX=10090
AT2A2_MOUSE	6	1	6-0-0-0	-			-			36.1	Aldose reductase-related protein 2	Mus musculus OX=10090
RS3_MOUSE	6	1	6-0-0-0	-			-			42.3	Calcium-binding and spermatid-specific protein 1	Mus musculus OX=10090
TCPZ_MOUSE	6	1	6-0-0-0	-			-			63.7	Cytoskeleton-associated protein 4	Mus musculus OX=10090
CAND1_MOUSE	5	1	5-0-0-0	-			-			191.6	Clathrin heavy chain 1	Mus musculus OX=10090
HYOU1_MOUSE	5	1	5-0-0-0	-			-			69.7	Dynein assembly factor 1, axonemal	Mus musculus OX=10090
PDIA1_MOUSE	5	1	5-0-0-0	-			-			49.2	Dynein regulatory complex protein 9	Mus musculus OX=10090
RPN1_MOUSE	5	1	5-0-0-0	-			-			26.8	EF-hand domain-containing protein D2	Mus musculus OX=10090
41_MOUSE	4	1	4-0-0-0	-			-			36.9	Fructose-1,6-bisphosphatase 1	Mus musculus OX=10090

CALM1_MOUSE	**4**	**1**	4-0-0-0	-			-			272.4	Fatty acid synthase	Mus musculus OX=10090
IPO5_MOUSE	**4**	**1**	4-0-0-0	-			-			13.3	Ig heavy chain V region 36-65	Mus musculus OX=10090
PDIA4_MOUSE	**4**	**1**	4-0-0-0	-			-			46.7	Platelet-activating factor acetylhydrolase IB subunit alpha	Mus musculus OX=10090
PRDX6_MOUSE	**4**	**1**	4-0-0-0	-			-			36.5	Malate dehydrogenase, cytoplasmic	Mus musculus OX=10090
PSD11_MOUSE	**4**	**1**	4-0-0-0	-			-			35.6	Malate dehydrogenase, mitochondrial	Mus musculus OX=10090
TPP2_MOUSE	**4**	**1**	4-0-0-0	-			-			39.6	Phosphate carrier protein, mitochondrial	Mus musculus OX=10090
XPP1_MOUSE	**4**	**1**	4-0-0-0	-			-			28.1	Thioredoxin-dependent peroxide reductase, mitochondrial	Mus musculus OX=10090
ALD2_MOUSE	**3**	**1**	3-0-0-0	-			-			44.2	26S proteasome regulatory subunit 10B	Mus musculus OX=10090
CABS1_MOUSE	**3**	**1**	3-0-0-0	-			-			29.5	Proteasome subunit alpha type-4	Mus musculus OX=10090
CLH1_MOUSE	**3**	**1**	3-0-0-0	-			-			29.1	Proteasome subunit beta type-4	Mus musculus OX=10090
DAAF1_MOUSE	**3**	**1**	3-0-0-0	-			-			105.7	26S proteasome non-ATPase regulatory subunit 1	Mus musculus OX=10090
DRC9_MOUSE	**3**	**1**	0-0-3-0	-			-			60.7	26S proteasome non-ATPase regulatory subunit 3	Mus musculus OX=10090
EFHD2_MOUSE	**3**	**1**	3-0-0-0	-			-			22.2	Ras-related protein Rab-1B	Mus musculus OX=10090
F16P1_MOUSE	**3**	**1**	3-0-0-0	-			-			23.6	60S ribosomal protein L14	Mus musculus OX=10090
FAS_MOUSE	**3**	**1**	3-0-0-0	-			-			16.3	40S ribosomal protein S14	Mus musculus OX=10090
LIS1_MOUSE	**3**	**1**	3-0-0-0	-			-			34.2	Radial spoke head 1 homolog	Mus musculus OX=10090
MDHC_MOUSE	**3**	**1**	3-0-0-0	-			-			170.1	Bifunctional glutamate/proline--tRNA ligase	Mus musculus OX=10090
MDHM_MOUSE	**3**	**1**	3-0-0-0	-			-			75.7	Arginine--tRNA ligase, cytoplasmic	Mus musculus OX=10090
PRDX3_MOUSE	**3**	**1**	3-0-0-0	-			-			71.2	Thioredoxin reductase 3	Mus musculus OX=10090
PRS10_MOUSE	**3**	**1**	3-0-0-0	-			-			85.5	Aconitate hydratase, mitochondrial	Mus musculus OX=10090
PSA4_MOUSE	**3**	**1**	3-0-0-0	-			-			11.2	Acylphosphatase-1	Mus musculus OX=10090
PSB4_MOUSE	**3**	**1**	3-0-0-0	-			-			36.6	Aldo-keto reductase family 1 member A1	Mus musculus OX=10090
PSMD1_MOUSE	**3**	**1**	3-0-0-0	-			-			93.8	A-kinase anchor protein 4	Mus musculus OX=10090
PSMD3_MOUSE	**3**	**1**	3-0-0-0	-			-			54.0	Aldehyde dehydrogenase family 3 member A2	Mus musculus OX=10090
RAB1B_MOUSE	**3**	**1**	3-0-0-0	-			-			42.4	Protein arginine N-methyltransferase 1	Mus musculus OX=10090
SYEP_MOUSE	**3**	**1**	3-0-0-0	-			-			50.5	Damage-control phosphatase ARMT1	Mus musculus OX=10090
SYRC_MOUSE	**3**	**1**	3-0-0-0	-			-			64.3	Asparagine synthetase [glutamine-hydrolyzing]	Mus musculus OX=10090
TRXR3_MOUSE	**3**	**1**	3-0-0-0	-			-			42.5	Cytosolic acyl coenzyme A thioester hydrolase	Mus musculus OX=10090
ACON_MOUSE	**2**	**1**	2-0-0-0	-			-			70.8	Carnitine O-acetyltransferase	Mus musculus OX=10090
AK1A1_MOUSE	**2**	**1**	2-0-0-0	-			-			78.2	Caprin-1	Mus musculus OX=10090
AKAP4_MOUSE	**2**	**1**	2-0-0-0	-			-			38.2	Sorbitol dehydrogenase	Mus musculus OX=10090
AL3A2_MOUSE	**2**	**1**	2-0-0-0	-			-			40.6	DnaJ homolog subfamily B member 11	Mus musculus OX=10090
ANM1_MOUSE	**2**	**1**	2-0-0-0	-			-			13.1	D-dopachrome decarboxylase	Mus musculus OX=10090
ARMT1_MOUSE	**2**	**1**	2-0-0-0	-			-			53.4	Dynein regulatory complex protein 10	Mus musculus OX=10090
ASNS_MOUSE	**2**	**1**	2-0-0-0	-			-			49.0	Spliceosome RNA helicase Ddx39b	Mus musculus OX=10090
BACH_MOUSE	**2**	**1**	2-0-0-0	-			-			24.7	Elongation factor 1-beta	Mus musculus OX=10090
CACP_MOUSE	**2**	**1**	2-0-0-0	-			-			28.8	Endoplasmic reticulum resident protein 29	Mus musculus OX=10090
CAPR1_MOUSE	**2**	**1**	2-0-0-0	-			-			32.5	Glucosamine-6-phosphate isomerase 1	Mus musculus OX=10090
DHSO_MOUSE	**2**	**1**	2-0-0-0	-			-			31.1	Glucosamine-6-phosphate isomerase 2	Mus musculus OX=10090
DJB11_MOUSE	**2**	**1**	2-0-0-0	-			-			23.6	Glutathione S-transferase P 1	Mus musculus OX=10090
DRC10_MOUSE	**2**	**1**	0-0-2-0	-			-			54.0	Solute carrier family 2, facilitated glucose transporter member 1	Mus musculus OX=10090
DX39B_MOUSE	**2**	**1**	2-0-0-0	-			-			11.6	High mobility group protein HMG-I/HMG-Y	Mus musculus OX=10090
EF1B_MOUSE	**2**	**1**	2-0-0-0	-			-			35.7	Heme oxygenase 2	Mus musculus OX=10090
ERP29_MOUSE	**2**	**1**	2-0-0-0	-			-			64.0	Heterogeneous nuclear ribonucleoprotein L	Mus musculus OX=10090
GNPI1_MOUSE	**2**	**1**	2-0-0-0	-			-			16.8	Eukaryotic translation initiation factor 5A-1	Mus musculus OX=10090
GNPI2_MOUSE	**2**	**1**	2-0-0-0	-			-			45.4	cAMP-dependent protein kinase type II-alpha regulatory subunit	Mus musculus OX=10090
GSTP1_MOUSE	**2**	**1**	2-0-0-0	-			-			50.8	LanC-like protein 2	Mus musculus OX=10090
GTR1_MOUSE	**2**	**1**	2-0-0-0	-			-			34.8	Leucine zipper transcription factor-like protein 1	Mus musculus OX=10090
HMOX2_MOUSE	**2**	**1**	2-0-0-0	-			-			34.1	NADH-cytochrome b5 reductase 3	Mus musculus OX=10090
IF5A1_MOUSE	**2**	**1**	2-0-0-0	-			-			113.1	Poly [ADP-ribose] polymerase 1	Mus musculus OX=10090

LANC2_MOUSE	**2**	**1**	2-0-0-0	-			-			67.8	Protein disulfide-isomerase-like protein of the testis	Mus musculus OX=10090
LZTL1_MOUSE	**2**	**1**	2-0-0-0	-			-			534.2	Plectin	Mus musculus OX=10090
NB5R3_MOUSE	**2**	**1**	2-0-0-0	-			-			34.5	Palmitoyl-protein thioesterase 1	Mus musculus OX=10090
PARP1_MOUSE	**2**	**1**	2-0-0-0	-			-			108.5	Pre-mRNA-processing factor 40 homolog A	Mus musculus OX=10090
PDILT_MOUSE	**2**	**1**	2-0-0-0	-			-			49.5	26S proteasome regulatory subunit 6A	Mus musculus OX=10090
PLEC_MOUSE	**2**	**1**	2-0-0-0	-			-			28.4	Proteasome subunit alpha type-3	Mus musculus OX=10090
PR40A_MOUSE	**2**	**1**	2-0-0-0	-			-			34.6	26S proteasome non-ATPase regulatory subunit 14	Mus musculus OX=10090
PRS6A_MOUSE	**2**	**1**	2-0-0-0	-			-			23.0	Ras-related protein Rab-18	Mus musculus OX=10090
PSA3_MOUSE	**2**	**1**	2-0-0-0	-			-			20.5	Ras-related protein Rap-2b	Mus musculus OX=10090
PSDE_MOUSE	**2**	**1**	2-0-0-0	-			-			24.9	60S ribosomal protein L10a	Mus musculus OX=10090
RAB18_MOUSE	**2**	**1**	2-0-0-0	-			-			17.8	60S ribosomal protein L12	Mus musculus OX=10090
RAP2B_MOUSE	**2**	**1**	2-0-0-0	-			-			17.7	60S ribosomal protein L23a	Mus musculus OX=10090
RL10A_MOUSE	**2**	**1**	2-0-0-0	-			-			69.1	Dolichyl-diphosphooligosaccharide--protein glycosyltransferase subunit 2	Mus musculus OX=10090
RL12_MOUSE	**2**	**1**	2-0-0-0	-			-			23.7	Small nuclear ribonucleoprotein-associated protein B	Mus musculus OX=10090
RL23A_MOUSE	**2**	**1**	2-0-0-0	-			-			32.8	40S ribosomal protein SA	Mus musculus OX=10090
RPN2_MOUSE	**2**	**1**	2-0-0-0	-			-			56.5	Succinyl-CoA:3-ketoacid coenzyme A transferase 2A, mitochondrial	Mus musculus OX=10090
RSMB_MOUSE	**2**	**1**	2-0-0-0	-			-			31.8	Succinate dehydrogenase [ubiquinone] iron-sulfur subunit, mitochondrial	Mus musculus OX=10090
RSSA_MOUSE	**2**	**1**	2-0-0-0	-			-			9.7	Small integral membrane protein 4	Mus musculus OX=10090
SCO2A_MOUSE	**2**	**1**	2-0-0-0	-			-			24.6	Superoxide dismutase [Mn], mitochondrial	Mus musculus OX=10090
SDHB_MOUSE	**2**	**1**	2-0-0-0	-			-			100.7	Sperm-associated antigen 1	Mus musculus OX=10090
SODM_MOUSE	**2**	**1**	2-0-0-0	-			-			62.6	Stress-induced-phosphoprotein 1	Mus musculus OX=10090
SPAG1_MOUSE	**2**	**1**	2-0-0-0	-			-			38.4	Serine-threonine kinase receptor-associated protein	Mus musculus OX=10090
STIP1_MOUSE	**2**	**1**	2-0-0-0	-			-			31.2	Syntaxin-12	Mus musculus OX=10090
STRAP_MOUSE	**2**	**1**	2-0-0-0	-			-			57.1	Aspartate--tRNA ligase, cytoplasmic	Mus musculus OX=10090
SYDC_MOUSE	**2**	**1**	2-0-0-0	-			-			140.2	Valine--tRNA ligase	Mus musculus OX=10090
SYVC_MOUSE	**2**	**1**	2-0-0-0	-			-			37.4	Transaldolase	Mus musculus OX=10090
TALDO_MOUSE	**2**	**1**	2-0-0-0	-			-			44.8	Acetyl-CoA acetyltransferase, mitochondrial	Mus musculus OX=10090
THIL_MOUSE	**2**	**1**	2-0-0-0	-			-			41.8	3-ketoacyl-CoA thiolase, mitochondrial	Mus musculus OX=10090
THIM_MOUSE	**2**	**1**	2-0-0-0	-			-			67.6	Transketolase	Mus musculus OX=10090
TKT_MOUSE	**2**	**1**	2-0-0-0	-			-			24.9	Transmembrane emp24 domain-containing protein 10	Mus musculus OX=10090
TMEDA_MOUSE	**2**	**1**	2-0-0-0	-			-			181.9	DNA topoisomerase 2-beta	Mus musculus OX=10090
TOP2B_MOUSE	**2**	**1**	2-0-0-0	-			-			109.4	116 kDa U5 small nuclear ribonucleoprotein component	Mus musculus OX=10090
UBP7_MOUSE	**2**	**1**	2-0-0-0	-			-			128.5	Ubiquitin carboxyl-terminal hydrolase 7	Mus musculus OX=10090
WDR92_MOUSE	**2**	**1**	2-0-0-0	-			-			39.8	WD repeat-containing protein 92	Mus musculus OX=10090

Tandem mass spectrometry (MS/MS) analysis was performed on TTC29-immunoprecipitated pellets obtained from wild-type and Ttc29$^{-/-}$ L5 and L7 mouse testes. N=4 for controls and N=4 for *TTC29*$^{-/-}$ mutants. 124 proteins were specifically identified in wild-type and absent from samples from both Ttc29$^{-/-}$ L5 and L7 mutants. Proteins are ranked by their total peptides count. Only three proteins were systematically identified in the four experimental replicates: DNAH1, DNALI1 and TTC29. For each protein, the total number of peptides is indicated alongside the distribution of peptides in each experimental replicate.

Table S3. Primer sequences for Sanger sequencing verification of *ZMYND12* variants.

Primers	Primer sequence (5'-3')	Tm (°C)	Product length (bp)
ZMYND12-F-Ex4	AGGCTGCTGTGAACATTCCT	57.3	250
ZMYND12-R-Ex4	AATGCTTGAACTCGGGTCGG	59.4	

Table S4. *ZMYND12* MLPA probes used in this work.

MLPA probes	Upstream hybridizing sequence (5'-3')	Downstream hybridizing sequence (5'-3')	Total probe length (nt)
***ZMYND12* specific probes**			
exons 5	GCTACTTCCACCTGGCTAATATATTCTATGACCTT	AAAAAGTTGGACCTGGCAGACACATTGTACACCAA	112
exon 6	GGTCTCTGAGATCTGGCATGCATATTTGAAC	AATCACTATCAAGTCCTCTCACAGGCTCACATCCA	108
exon 8	CTCAGTCTAGCCAAAGAACAACAGCTTGA	TGTCCATGAGCAAAGCACCATTCAAGAGT	98

For each probe, the unique hybridizing sequence of the two half-probes is given. Total probe length represents the total length of amplification product (nt=nucleotides) = forward primers + upstream hybridizing sequence + downstream hybridizing sequence + reverse primers.

Table S5. Primers used for RT-qPCR detection of *ZMYND12* in human tissue extracts.

Primer names	Primer sequences (5'-3')	Tm
ZMYND12_RT_F	TACTGCATCGGAATCTGGGAC	59 °C
ZMYND12_RT_R	GCCAGATGATAACGGGCCTC	
RPL6_RTqPCR_F	TCCATTCGTCAGAGCAAACA	56 °C
RPL6_RTqPCR_R	TACGGAGCAGCGCAAGAT	
RPL27_RTqPCR_F	AGAGTACCTTGTGGGCAT	56 °C
RPL27_RTqPCR_R	TGATGGCACCTCAGATCGC	

Tm: melting temperature

Table S6. Primary antibodies used in immunofluorescence experiments with human samples

Primary antibodies	Reference	Species	Localization	Dilution
Human experiments				
AKAP4	Sigma-Aldrich® HPA020046	Rabbit	Fibrous sheath	1/100
CFAP70	Sigma-Aldrich® HPA062453	Rabbit	Unknown (base of ODA?)	1/50
DNAH1	Sigma-Aldrich® HPA036806	Rabbit	IDA	1/25
DNAH17	Sigma-Aldrich® HPA024354	Rabbit	ODA	1/200
DNAH8	Sigma-Aldrich® HPA028447	Rabbit	ODA	1/200
DNAI1	Sigma-Aldrich® HPA021649	Rabbit	ODA	1/200
DNALI1	Sigma-Aldrich® HPA028305	Rabbit	IDA	1/100
GAS8	Sigma-Aldrich® HPA041311	Rabbit	N-DRC	1/100
RSPH1	Sigma-Aldrich® HPA017382	Rabbit	RS	1/100
SPAG6	Sigma-Aldrich® HPA020046	Rabbit	CPC	1/500
TTC29	Sigma-Aldrich® HPA061473	Rabbit	Unknown (IDA? IFT?)	1/100
WDR66	Sigma-Aldrich® HPA040005	Rabbit	CSC	1/20
ZMYND12(PA5-69715)	Sigma-Aldrich® HPA062453	Rabbit	Unknown	1/100
β-tubulin	Cell signal 2128	Rabbit	microtubules	1/500
β-tubulin	Sigma-Aldrich® T4026	Mouse	microtubules	1/500

Abbreviations: ODA, Outer Dynein Arms; IDA, Inner Dynein Arms; RS, Radial Spokes; FS, Fibrous sheath; CPC, Central Pair Complex; N-DRC: Nexin-Dynein Regulatory Complex, CSC: calmodulin-associated and spoke-associated complex

Table S7. Primary antibodies used in immunofluorescence experiments with *Trypanosoma* cells

Antibody	Provider & Reference	Dilution IF	Dilution U-ExM	WB Dilution	IP Dilution
Primary antibodies					
Anti-PFR2	(Coutton et al., 2018)	1:500	-	-	-
Anti-TbSAXO	(Dacheux et al., 2012)	1:1000	-	1:1000	
Anti-Myc	Mouse monoclonal 9E10	1:1000	-	-	-
Anti-Myc	Sigma c-3956	-	-	1:1000	-
Anti-Ty1 (purified supernatant)	(Brookman et al., 1995)	1:2000	1:500	1:10,000	1:33
Anti-HA	Genetex GTX628902	-	-	-	1:50
Anti-Enolase	(Hannaert et al., 2003)	-	-	1:25,000	
Anti-Tubulin	(Woods et al., 1989)	-	-	1:1000	-
Secondary antibodies					
Anti-mouse FITC	Sigma F2012	1:100	-	-	-
Anti-rabbit Alexa fluor 594	Molecular Probes A21201	1:200	-	-	-
Anti-rabbit Alexa fluor A647	Molecular Probes A31573	-	1:500	-	-
Anti-mouse Alexa fluor A488	Molecular Probes A11001	-	1:500	-	-
Anti-mouse HRP	Jackson 115-035-062	-	-	1:10,000	-
Anti-rabbit HRP	Sigma A-9169	-	-	1:10,000	-
Anti-rabbit StarBright Blue 700	Bio-Rad 12004162	-	-	1:2500	-
Anti-mouse StarBright Blue 520	Bio-Rad 12005867	-	-	1:2500	-

Movie S1. Video microscopy of WT cells.

Movie S2. Video microscopy of RNAi$^{TbTAX\text{-}1}$ cells 7 days post-induction.